Mechanisms Driving Ocean Heat Uptake and Warm Water Volume Variability over Idealized ENSO Events

Master Thesis in Atmospheric and Climate Science

by

Maurice Huguenin-Virchaux

at the Climate Change Research Centre, UNSW Sydney

Supervisors:

Dr. Ryan Holmes - ryan.holmes@unsw.edu.au
Prof. Dr. Matthew H. England - m.england@unsw.edu.au
Dr. Iselin Medhaug - iselin.medhaug@env.ethz.ch
Prof. Dr. Reto Knutti - reto.knutti@env.ethz.ch

9th April 2018

Abstract

The El Niño-Southern Oscillation (ENSO) is the most pronounced variation of the Earth's climate system on the interannual time scale. To a first order, ENSO can be described as a harmonic oscillator with symmetric and opposite El Niño and La Niña events. Ocean heat content (OHC) and its associated warm water volume (WWV) are good indicators for the state of the ocean throughout ENSO. In this study, the variability of OHC and WWV is simulated in a global ocean-sea ice model over symmetric El Niño, La Niña and full ENSO cycles to investigate how non-linear ocean processes lead to asymmetries in these two metrics. OHC anomalies at the peak of El Niño and La Niña reveal that the global ocean at 200m depth warms considerably more during La Niña than it cools during El Niño. The asymmetric vertical motion of the thermocline (TC) in the western Pacific warm pool is identified as the main mechanism responsible for this asymmetry. While OHC asymmetries are strongest in the western equatorial Pacific, the processes responsible for depletion (during El Niño) and build-up (during La Niña) of OHC are strongest in the eastern Pacific. Decomposing the WWV balance in the equatorial Pacific 5°N–5°S reveals two stages during its discharge and recharge; an initial stage driven by diabatic volume fluxes followed by strong adiabatic volume fluxes three months later. During discharge, both surface forcing and vertical mixing contribute 40% of the WWV depletion. These diabatic changes are caused by weaker trade winds, a warmer sea surface temperature and less turbulence above the TC. Following this change, the second stage controlled by adiabatic transport out of the equatorial region contributes the remaining 60%. This lag by three months, due to the required southward shift in wind anomalies during the latter stages of El Niño, causing basin-wide northward Ekman transport. During the initial recharge phase, strong surface forcing is responsible for most of the added WWV due to stronger trade winds, enhancing heat absorption of upwelled cold water masses. In contrast, vertical mixing, as during El Niño, is depleting anomalous WWV at this time. This is the result of the upward shift of the eastern Pacific TC toward the surface where strong mixing cools water masses. Together, these diabatic fluxes contribute approximately 60% to the total WWV recharge. Comparable to El Niño, the first stage during La Niña's discharge is followed by meridional transport into the equatorial region contributing the remaining 40% of WWV. The results here have implications for understanding the cycling of heat over ENSO events, highlighting the importance of diabatic processes in the form of surface heat fluxes and vertical mixing.

"We learned a lot about the Moon, but what we really learned was about the Earth. The fact that just from the distance of the Moon you can put your thumb up and you can hide the Earth behind your thumb. Everything that you've ever known, your loved ones, your business, the problems of the Earth itself — all behind your thumb. And how insignificant we really all are, but then how fortunate we are to have this body and to be able to enjoy living here amongst the beauty of the Earth itself."

— Jim Lovell, Apollo 8 and 13 Astronaut.

Acknowledgments

I would like to first thank Ryan Holmes for always taking the time to answer my questions and for his great support throughout this project. It was a big help when he visited my desk to discuss my current progress. His detailed and constructive comments to my draft report were of great help. I would also like to thank Prof. Matthew England for his inputs and his time to meet with me and Ryan each week in person and even online when he was travelling abroad. Getting their valuable inputs to my figures was always a good motivation to proceed and to improve the way I presented results of my simulations. My thanks also go to Iselin Medhaug and Reto Knutti helping me with any questions I had in organizing this project and allowing me to write my thesis in Australia. I also thank Iselin for the many useful inputs to my draft version and for always being supportive in her phone calls and emails. I also thank my family and especially my parents for their unconditional support in pursuing my academic interests.

Symbols and Abbreviations

Symbols

$\Delta\Theta$	Temperature dimension difference	[K]
Δz	Vertical grid cell difference	[m]
λE	Latent heat flux	$[\mathrm{W\,m^{-2}}]$
μ	Location parameter	
ν	Kinematic viscosity of sea water	$[\mathrm{m^2\,s^{-1}}]$
ρ_a	Reference air density	$[\mathrm{kg\,m^{-1}}]$
ρ_0	Density of sea water at the surface	$[\mathrm{kg\,m^{-3}}]$
σ	Standard deviation	
σ^2	Variance	
Σ	Covariance matrix	
θ	Potential temperature of sea water	[°C]
Θ	Conservative temperature of sea water	[K]
$\vec{\tau}^T$	Transposed wind stress vector	$[\mathrm{N\,m^{-2}}]$
τ_x	Zonal wind stress	$[\mathrm{N\,m^{-2}}]$
τ_y	Meridional wind stress	$[\mathrm{N\,m^{-2}}]$
ω	Time dimension	
a	Area in the WWV region	$[\mathrm{m^2}]$
C_D	Drag coefficient	
C_e	Transfer coefficient for latent heat	
C_h	Transfer coefficient for sensible heat	
c_p	Specific heat capacity of sea water	$[\mathrm{J\,kg^{-1}\,K^{-1}}]$
EOF	Spatial pattern of EOF analysis	
F	Forcing field	
$F_{ideal.}$	Idealized forcing field	
F_{ICE}	Heat flux due to ice melting	$[\mathrm{W\,m^{-2}}]$
$F_{LW}^{\downarrow}$	Downward long-wave radiative flux	$[\mathrm{W\,m^{-2}}]$
$F_{SW}^{\downarrow}$	Downward short-wave radiative flux	$[\mathrm{W\,m^{-2}}]$
$\mathcal{F}$	Surface forcing heat flux	$[\mathrm{W\,m^{-2}}]$
$\mathcal{G}_{\mathcal{F}}$	Volume flux due to surface forcing	$[\mathrm{m^3\,s^{-1}}]$
$\mathcal{G}_{\mathcal{I}}$	Volume flux due to implicit mixing	$[\mathrm{m^3\,s^{-1}}]$
$\mathcal{G}_{\mathcal{M}}$	Volume flux due to vertical mixing	$[\mathrm{m^3\,s^{-1}}]$
h	Thermocline depth anomaly in the central Pacific	[m]
i	Control variable	
$\mathcal{J}$	Volume flux due to surface volume flux	$[\mathrm{m^3\,s^{-1}}]$
k	Constant combining ρ_a and C_D	$[\mathrm{kg\,m^{-3}}]$
l	Total zonal wind stress forcing	$[\mathrm{N\,m^{-2}}]$

m	Total meridional wind stress forcing	$[\mathrm{N\,m^{-2}}]$
$\mathcal{M}$	Vertical mixing heat flux	$[\mathrm{W\,m^{-2}}]$
MSD	Monthly standard deviation	
N	Total number of time steps	
$N34$	Niño3.4 index	$[^{\circ}\mathrm{C}]$
OHC	Ocean heat content	[J]
p	Number of EOFs	
PC	Principle component time series	
q_v	Specific humidity	$[\mathrm{kg\,kg^{-1}}]$
q_{sat}	Saturation water vapour mixing ratio	$[\mathrm{kg\,kg^{-1}}]$
Q	Heat flux	$[\mathrm{W\,m^{-2}}]$
$Q_{net}^{\downarrow}$	Downward net surface heat flux	$[\mathrm{W\,m^{-2}}]$
r	Correlation coefficient	
R	Precipitation or rain rate	[mm]
S_A	Absolute salinity	$[\mathrm{g\,kg^{-1}}]$
SH	Sensible heat flux	$[\mathrm{W\,m^{-2}}]$
SOI	Southern oscillation index	
SLP	Sea level pressure	[Pa]
s	Scale parameter	
$st.\,Darwin$	standardized SLP in Darwin	[Pa]
$st.\,Tahiti$	standardized SLP in Tahiti	[Pa]
Sv	Volumetric flux	$[10^6\,\mathrm{m^3\,s^{-1}}]$
t	Time dimension	
T	Air temperature	[K]
u	Zonal wind speed	$[\mathrm{m\,s^{-1}}]$
U	Wind speed magnitude	$[\mathrm{m\,s^{-1}}]$
v	Meridional wind speed	$[\mathrm{m\,s^{-1}}]$
V	Meridional flux of sea water	$[\mathrm{m^3\,s^{-1}}]$
$\mathcal{V}$	Global sea water volume	$[\mathrm{m^3}]$
w'	Turbulent vertical wind velocity	$[\mathrm{m\,s^{-1}}]$
WWV	Warm water volume	$[\mathrm{m^3}]$
x	Zonal dimension	
$X_{1,2}$	Regression pattern associated with $N34$, PC	
y	Meridional dimension	
z	Depth dimension	

Abbreviations

CNYF	Coordinated Ocean-ice Reference Experiment Normal Year Forcing
EN	El Niño
ENSO	El Niño–Southern Oscillation
EXP	Experiment
EOF	Empirical Orthogonal Function
GMSST	Global Mean Sea Surface Temperature
IOD	Indian Ocean Dipole
ITF	Indonesian Throughflow
LN	La Niña
MSD	Monthly Standard Deviation
mEN	Moderate El Niño
mLN	Moderate La Niña
NOAA	National Oceanographic and Atmospheric Administration
N34	Niño3.4 index
OHC	Ocean Heat Content
PC	Principle Component
RDO	Recharge–Discharge Oscillator
SSH	Sea Surface Height
SST	Sea Surface Temperature
Sv	Sverdrup (Volumetric unit of transport)
TC	Thermocline
WMT	Water Mass Transformation
WWV	Warm Water Volume
WPWP	Western Pacific Warm Pool

Contents

1

Introduction

The El Niño-Southern Oscillation (ENSO) is a coupled ocean-atmosphere phenomenon in the equatorial Pacific and the most pronounced variation in the Earth's climate system on an interannual time scale. Among others, the oceanic part of the oscillation leads to large-scale changes in sea surface temperature (SST) and ocean heat content (OHC) while the atmospheric part includes changes in the large-scale circulation (Collins et al., 2010). Impacts including droughts, heat waves, heavy rainfall, storms and changes in the frequency of hurricanes are felt around the globe (Diaz et al., 2001; Smith et al., 2007). To better predict ENSO events and their impacts, an increased understanding of their underlying physical processes is necessary.

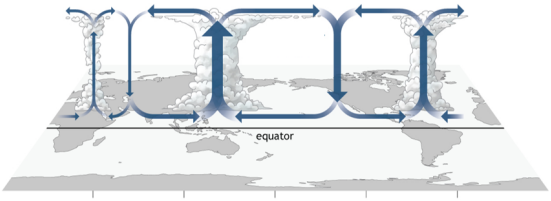

Figure 1.1: Simplified Walker circulation in the equatorial Pacific during normal conditions. Large-scale ascent of air masses over the warm western Pacific leads to convection and upper-tropospheric flow into the Indian and the eastern Pacific Ocean. Descent in the eastern Pacific is driven by the cold SST creating a low surface pressure anomaly. The westward blowing trade winds close the circulation loop. Drawing by Fiona Martin from NOAA.gov.

During normal conditions in the equatorial Pacific, westward blowing trade winds lead to surface water masses continuously being transported away from the Equator as a result of the Coriolis force (Ekman, 1905). Net transport is to the left of the wind direction in the Southern Hemisphere and to the right in the Northern Hemisphere (Ekman, 1905). The transport away from the Equator is balanced by upwelling of cold water masses from below. In the Western Pacific Warm Pool (WPWP), SST values are higher as surface heat fluxes continuously warm water masses. This East-West, cold-warm SST contrast drives the large-scale atmospheric circulation pattern; the Walker circulation. Large-scale ascent over the warm

Pacific Ocean in the West and subsequent descent over the cooler eastern Pacific drives the trade winds at the surface (Figure 1.1) which maintain the SST gradient (i.e. the positive Bjerknes feedback loop (Bjerknes, 1969)).

The climate indices Oceanic Niño Index (ONI) for the oceanic part and the Southern Oscillation Index (SOI) for the atmospheric part of ENSO are among the most commonly used to assess its evolution and current state. The ONI is calculated as the 3–month running mean SST deviation in the Niño3.4 region (5°S–5°N and 170°E–120°W) based on a 30–year climatological period (NOAA CPC (2017), Figure 1.2a). A climatological period is used to derive the mean annual state of the Earth's climate as a reference for calculating anomalies. In this study, the climatological period is 1971–2000. An El Niño (La Niña) event is defined as a departure of greater or equal to +0.5°C (−0.5°C) for at least five consecutive overlapping 3–month seasons. The SOI index is calculated as the standardized pressure anomaly difference between Tahiti (French Polynesia) and Darwin (Australia) relative to the 1981–2010 climatological period ((NOAA CPC, 2017), Figure 1.2b, for the calculation see Section A.1). The two indices have a strong negative correlation with a coefficient of $r = -0.83$ meaning that negative values of SOI often indicate an El Niño event and vice versa for La Niña. These two indices show the strong coupling between ocean and atmosphere through the Bjerknes feedback and the 2–7 year time-scale of ENSO (Meinen and McPhaden, 2000).

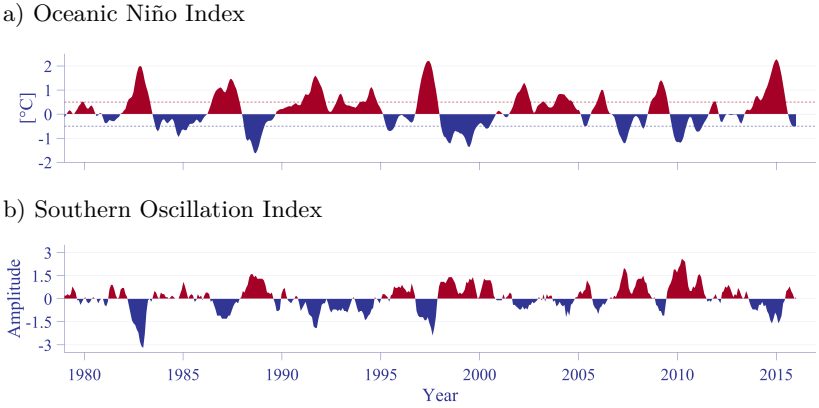

Figure 1.2: In a) the time evolution of the observed ONI [°C] and in b) for the observed SOI. Positive anomalies are shown in red and negative anomalies in blue. The dashed red (blue) line in a) indicates the threshold of +0.5°C (−0.5°C) which has to be exceeded for five consecutive months for an event to be classified as an El Niño (La Niña). The data is downloaded from the National Oceanographic and Atmospheric Administration's Climate Prediction Center (NOAA CPC, 2017).

The most important dynamics of ENSO can be understood using the Recharge-Discharge Oscillator (RDO) theory by Jin (1997). Under the RDO theory, an idealized ENSO cycle can be defined as a delayed harmonic oscillator with two key metrics: the anomalous thermocline (TC, i.e. the separation at 20°C between warm and cold water masses) in the central Pacific h and the SST anomaly in the eastern Pacific SST_a (Figure 1.3). In addition, the anomalous Walker circulation is given as the anomalous wind stress (i.e. the force enacted by the wind on the ocean's surface) in the western equatorial Pacific. ENSO as a harmonic oscillator is divided into four different phases: El Niño and La Niña states as well as two transition states of neutral atmospheric surface conditions.

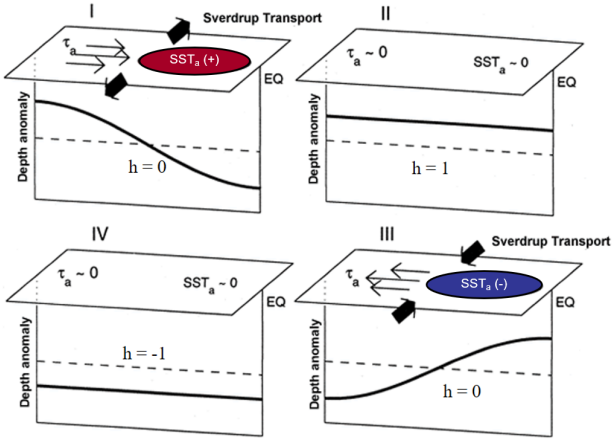

Figure 1.3: Idealized schematic as a summary of the ENSO Recharge–Discharge Oscillator theory from Meinen and McPhaden (2000): "All shown quantities are anomalies relative to the climatological mean. The bold line represents the depth anomaly of the TC. SST_a and τ_a [and h] denote sea surface temperature, zonal (East–West) wind stress [and the TC depth] anomalies. The bold arrows show meridional (North–South) transport of warm water masses to [from] higher latitudes during El Niño [La Niña]. An oscillation acting on a 2–7 year time scale follows the panel numbering [with I (III) representing El Niño (La Niña) conditions]."

The onset of El Niño occurs when trade winds weaken due to westerly wind anomalies in the western Pacific. The wind stress anomalies excite perturbations in the TC depth, causing equatorially trapped eastward (westward) propagating Kelvin (Rossby) waves with a group speed of ∼2.8 (∼0.9) $\mathrm{m\,s^{-1}}$ (Wang et al., 2016). These Kelvin waves lead to the transport of warm water masses from the WPWP to the East (Stewart, 2008) and a subsequent shift in warm SST values eastward. Following the spatial pattern of SST val-

ues, the Walker circulation shifts eastward with ascent in the central Pacific instead of the western Pacific.

The reduced strength of the atmospheric circulation leads to decreased upwelling of cold water masses in the East and subsequent warming of surface water masses there (McPhaden et al. (2006), Panel I in Figure 1.3). In addition, the equatorial Pacific warm water volume (WWV, i.e. the volume of water above 20°C in the region 5°S–5°N and 120°E–80°W) also increases by horizontal transport into the region prior to the peak of El Niño (Lengaigne et al., 2012).

The El Niño event peaks when the warm water masses reach the eastern Pacific and are exposed at the surface. Most of the accumulated heat is being discharged out of the equatorial region by either horizontal or vertical volume fluxes. The model-based study by Lengaigne et al. (2012) suggests that horizontal transport contributes approximately 60% to the total WWV decrease while the remaining ∼40% are due to the heat release into the atmosphere and vertical mixing into the ocean's interior across the TC. Furthermore, McGregor et al. (2014) show that transport out of the equatorial band 5°N–5°S is meridionally asymmetric due to stronger wind stress anomalies and subsequent Ekman transport in the Southern Hemisphere.

As WWV anomalies decrease, subsurface layers cool and correspondingly the TC shallows (panel II, Figure 1.3). The end of an El Niño event most often coincides with the meeting of Kelvin and Rossby waves after they are reflected at the eastern and western boundaries of the tropical Pacific basin respectively. On average, it takes one year for the waves excited at the start of an El Niño to travel across the Pacific, to be reflected at the boundaries and to meet again (Stewart, 2008).

Upwelling slowly resumes at the eastern boundary when trade winds return to their normal strength (as indicated by $\tau_a \sim 0$ in panel III, Figure 1.3). Cold water masses once again reach the surface and reduce local SST values back to normal conditions. Through the Bjerknes feedback, the Walker circulation strengthens and extends into the western Pacific once more.

During La Niña events with stronger than average easterly trade winds, cool SST values are enhanced (panel III in Figure 1.3). The accelerated trade winds intensify equatorial upwelling of cold water masses which take up large amounts of excess heat from the atmosphere (Meehl et al., 2011; Roemmich and Gilson, 2011). This heat is primarily stored in the mid-depth layers of the western Pacific as these water masses flow adiabatically along density

surfaces into the ocean's interior and recharge the WWV (Lengaigne et al., 2012). A subsequent El Niño event will then once again lead to discharge of this anomalous heat closing the oscillation loop.

While observational studies by Meinen and McPhaden (2000, 2001); Bosc and Delcroix (2008) and McPhaden (2012) are able to confirm the general characteristics of the RDO theory, much about the changes in WWV throughout ENSO is still unknown. Limited data availability, the difficulty to isolate ENSO from other internal modes of variability and the complexity to separate vertical heat fluxes affecting WWV in standard observational products constrain the current understanding (Meinen and McPhaden, 2001). However, increased knowledge of the underlying physical processes governing these WWV anomalies is key as it is a primary source for ENSO event prediction (NOAA CPC, 2017).

With the help of climate models, it is possible to assess the influence of different processes driving WWV anomalies during symmetric ENSO events as in the RDO theory. In this study, a global ocean-sea ice model is forced with a prescribed idealized atmospheric state representing a strong El Niño and its exact opposite. The simulations allow for the first time to investigate the asymmetric ocean heat response and show how the ocean deviates from the idealized RDO theory. Simulating ENSO cycles with symmetric atmospheric states reveal how ocean-sourced non-linearities lead to residual heat signals after atmospheric conditions return to climatological values.

Furthermore, the Water Mass Transformation (WMT) framework by Walin (1982) and improved by Iudicone et al. (2008) is used to separate horizontal from vertical processes affecting WWV and to investigate the different vertical components independently. While Lengaigne et al. (2012) successfully show how horizontal and vertical volume fluxes affect interannual variations in WWV, they did not investigate which vertical processes were most important.

This thesis is organised as follows: In Chapter 2, the ocean-sea ice model and the required data for the atmospheric forcing will be first described (Sections 2.1, 2.2). To simulate idealized ENSO events, an approach with Empirical Orthogonal Functions (EOFs) similar to McGregor et al. (2014) is used. In constrast to the aforementioned study, idealized ENSO-related time series instead of the full time series from the EOF analysis are used to drive isolated and symmetric events (Section 2.3). Atmospheric forcing is required for the parameterization of surface wind stress, heat and momentum fluxes which is shortly discussed in Sections 2.4 and in the Appendix in Section A.3.

The results from the isolated El Niño and La Niña events as well as the full ENSO cycles are presented in two parts in Chapter 3: OHC anomalies and their asymmetries between the peak of El Niño and La Niña and at the end of full ENSO cycles will be investigated first (Section 3.1). In the second part of Chapter 3, the WWV balance is established and analysed over the climatological seasonal cycle and over ENSO.

2

Model, Data and Methods

This chapter describes the ocean sea-ice model (Section 2.1), the datasets required to derive the atmospheric forcing (Section 2.2) as well as the statistical methods used in this study (Section 2.3).

2.1 The Ocean-Sea Ice Model

This study uses the GFDL-MOM025 global ocean and sea-ice model based on the Geophysical Fluid Dynamics Laboratory CM2.5 coupled climate model (Delworth et al., 2012). The model's grid cell resolution is $1/4^{\circ}$ with 50 vertical depth levels in a Cartesian coordinate system (Delworth et al., 2012). Atmospheric forcing is derived from a prescribed atmospheric state using eight fields to calculate zonal and meridional wind stress and by using bulk formulae in Fairall et al. (1996) surface heat and freshwater fluxes.

Prior to this study, the model was spun-up from rest over a 550–year period using the coordinated ocean-ice reference experiment normal year forcing (CNYF, (Large and Yeager, 2004). Repeated annual cycles of the CNYF are applied to obtain an equilibrated climatological average state, characterized by neutral ENSO conditions and neutral states of other climate modes (Large and Yeager, 2004; Maher et al., 2017).

2.2 Datasets

NOAA ERSST v4: The monthly sea surface temperature anomalies used to calculate the Niño3.4 index for the time period 1979–2016 are derived from NOAA's Extended Reconstruction Sea Surface Temperature version 4 (Smith and Reynolds, 2003) [1]. Anomalies are downloaded directly and are computed with respect to a 1971–2000 monthly climatology.

[1] https://www.ncdc.noaa.gov/data-access/marineocean-data/extended-reconstructed-sea-surface-temperature-ersst-v4.

NOAA SOI: The Southern Oscillation Index is directly downloaded from NOAA's Climate Prediction Centre (Ropelewski and Jones, 1987)[2]. See Section A.1 for the calculation of the SOI.

NOAA CNYF v2: The climatological atmospheric forcing is taken from NOAA's CNYF and includes the fields for 10 meter zonal and meridional wind speed, air temperature, specific humidity, downward long- and short-wave radiative fluxes, precipitation and sea level pressure (Large and Yeager, 2004)[3].

ERA-Interim: The additional forcing added to the control CNYF forcing to simulate the idealized ENSO events is derived from ERA-Interim data. The eight atmospheric forcing fields are downloaded as 6–hourly data from the European Center for Midrange Weather Forecast webpage for the time period 1979–2016 (Dee et al., 2011)[4]. Table 2.1 lists all fields necessary for the model input as well as additionally required fields.

Symbol	Unit	Description
u_{10}	$[\mathrm{m\,s^{-1}}]$	Zonal (East–West) wind speed at 10 m
v_{10}	$[\mathrm{m\,s^{-1}}]$	Meridional (North–South) wind speed at 10 m
T_{10}	[K]	Air temperature at 10 m
$q_{v,10}$	$[\mathrm{kg\,kg^{-1}}]$	Specific humidity at 10 m
$F^{\downarrow}_{LW}$	$[\mathrm{W\,m^{-2}}]$	Downward long-wave radiative flux at the surface
$F^{\downarrow}_{SW}$	$[\mathrm{W\,m^{-2}}]$	Downward short-wave radiative flux at the surface
R	[mm]	Precipitation or rain rate at the surface
SLP	[Pa]	Sea level pressure
Additional Fields		
$T_{d,10}$	[K]	Dew point temperature at 10 m
τ_x	$[\mathrm{N\,m^{-2}}]$	Zonal wind stress
τ_y	$[\mathrm{N\,m^{-2}}]$	Meridional wind stress

Table 2.1: The eight atmospheric fields for the model input from the Era-Interim product as well as the additionally required fields.

[2] http://www.cpc.ncep.noaa.gov/data/indices/.
[3] http://data1.gfdl.noaa.gov/nomads/forms/core/COREv2/CNYF_v2.html.
[4] https://www.ecmwf.int/en/forecasts/datasets/reanalysis-datasets/era-interim.

Monthly anomalies are calculated from 6–hourly data by detrending, removing the seasonal signal and calculating the monthly mean values. All fields are downloaded on a $^3/_4^\circ$ grid and linearly interpolated to the model's input grid cell resolution of 1.85°.

Air and dew point temperature are only available at 2 m. It is assumed that using these fields rather than fields at 10 m as required in the model results in a negligible difference.

Specific humidity is calculated with the equation given in Bolton (1980) from sea level pressure and dew point temperature (Equation 2.1).

$$q_v = \frac{0.622 \cdot a}{(SLP \cdot 10^{-2}) - (0.378 \cdot a)} \mid a = 6.112 \cdot e^{\left(\frac{17.67 \cdot (T_d - 273.15)}{(T_d - 273.15) + 243.5}\right)} \tag{2.1}$$

where SLP is in units of millibar [10^{-2} Pa] and T_d in [°C].

In addition, the two wind stress fields are required to calculate the correct wind speed input as will be discussed later in Section 2.4. Wind stresses are downloaded as monthly instead of 6–hourly values.

2.3 Development of Idealized Atmospheric Forcing

In order to simulate idealized ENSO events, a statistical analysis of the atmospheric data sets following McGregor et al. (2014) is used. This analysis results in spatial patterns and associated time series each representing a subset of variability within the data and thus allows to extract only the dominant ENSO-related signal in the tropical Pacific. As in McGregor et al. (2014), NOAA's ERSST v4 Niño3.4 index (N34) is regressed in Equation 2.2 onto the Era-Interim wind stress anomalies.

$$X_{1,\vec{\tau}}(x,y) = \frac{1}{N} \cdot \sum_{t=1}^{N} \frac{\vec{\tau}(x,y,t) \cdot N34(t)}{\sigma^2[N34(t)]} \qquad t = 1, \cdots, n \tag{2.2}$$

where $X_{1,\vec{\tau}}$ is the resulting spatial pattern with zonal and meridional wind stress components, N is the number of timesteps (456 months), $\vec{\tau}(x,y,t) = [\tau_x(x,y,t), \tau_y(x,y,t)]$ is the wind stress anomaly field with zonal and meridional components and $\sigma^2(N34)$ is the standard deviation of N34.

A very similar pattern and time series would result from an EOF analysis with the same dataset. An EOF analysis includes calculating spatial patterns

(i.e. $EOF_1(x, y)$, $EOF_2(x, y)$, etc.) and associated principle component time series (defined as $PC_1(t)$, $PC_2(t)$, etc.), each representing a percentage of variability within the data. The original variability can be reconstructed as in a linear model (Equation 2.3).

$$\vec{\tau}(x, y, t) = EOF_1 \cdot PC_1 + EOF_2 \cdot PC_2 + \cdots + \epsilon_i. \tag{2.3}$$

where ϵ_i is the error term or the difference between the original data and the value from the linear model.

Calculating EOF_1 and PC_1 of the wind stress anomalies instead of regressing the Niño3.4 index gives a time series which is highly correlated with N34 (correlation coefficient $r = 0.76$). As the smoother N34 timeseries was used in the study by McGregor et al. (2014) it is also utilized here.

The first pattern $X_{1,\vec{\tau}}$ captures the equatorially symmetric weakening of the Walker circulation during an El Niño event (Figure 2.1a). It is characterized by westerly wind stress anomalies in the western tropical Pacific with slightly larger values in the Southern Hemisphere.

To calculate the second pattern, the zonal and meridional wind stress anomalies associated with $X_{1,\vec{\tau}}$ are first removed from the wind stress anomaly time series at each spatial location and the first EOF of the residual wind stress over the tropical Pacific region 10°N–10°S and 100°E–60°W is calculated. This region is chosen as it includes the area where ENSO-related wind stress anomalies are strongest and is identical to the one in McGregor et al. (2014).

The EOF analysis includes two steps: First, the covariance matrix $\Sigma_{\vec{\tau}}$ containing key patterns of variability within the residual wind stress anomaly dataset is calculated (Equation 2.4). As a second step, the solution to the Eigenvalue problem is determined (Equation 2.5).

$$\Sigma_{\vec{\tau}}(x, y, t) = \frac{1}{N-1} \cdot \vec{\tau}^T(x, y, t) \cdot \vec{\tau}(x, y, t) \tag{2.4}$$

$$\Sigma_{\vec{\tau}}(x, y, t) \cdot EOF_i(x, y) = PC_i(t) \cdot EOF_i(x, y) \qquad i = 1, \cdots, p \tag{2.5}$$

where $\Sigma_{\vec{\tau}}(x, y, t)$ is the covariance matrix of the wind stress, $\vec{\tau}^T(t)$ is the transposed wind stress anomaly field, EOF_i is the i-th pattern, PC_i its associated amplitude and p is the number of principle components. These equations are based on the Manual for EOF and SVD Analyses of Climatic Data by Björnsson and Venegas (1997). While the first six EOF patterns

and their time series are statistically significant on the 5% level, only the first pair as in McGregor et al. (2014) is calculated. These patterns and time series are defined as $X_{2,\bar{\tau}}$ and PC.

$X_{2,\bar{\tau}}$ captures a strong meridional gradient of zonal wind across the equator. The southward shift in the westerly wind anomalies, when this pattern changes sign during El Niño, plays an important role in terminating it (Stuecker et al., 2015). This mode drives 17.1% of the variability within the residual wind stress anomaly dataset which is identical to the study by McGregor et al. (2014) using data for 1979–2011.

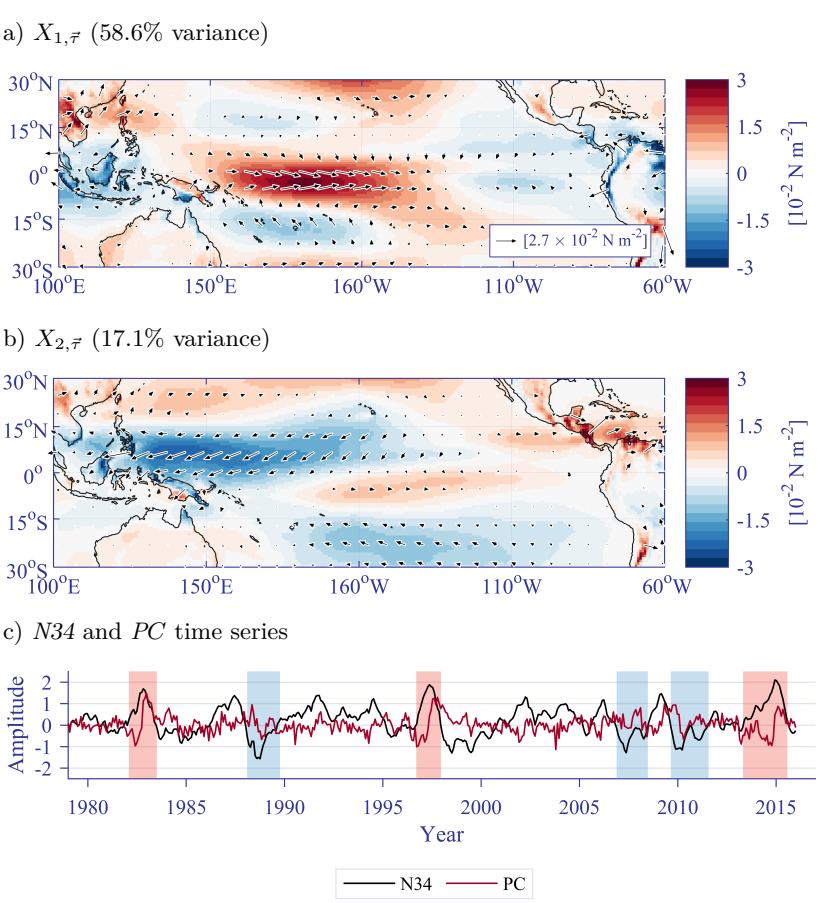

Figure 2.1: In a) the first and in b) the second mode of wind stress variability related to ENSO [10^{-2} N m^{-2}]. The zonal wind stress component is shaded. In c) the associated time series with *N34* in black and *PC* in red. Both patterns and time series are scaled with their standard deviation as in McGregor et al. (2014). Red (blue) shaded areas indicate the duration of the three strongest El Ninõ (La Niña) events.

2.3.1 Idealized ENSO-related Time Series

The study by McGregor et al. (2014) used the two time series N34 and PC (Figure 2.1c) to simulate the variability of the tropical Pacific over time period 1979–2011. Instead of using the full time series, idealized synthetic time

series for N34 and PC are constructed here to simulate individual El Niño and La Niña events (e.g. red shaded time periods in Figure 2.1c). Hereby, the evolution of N34 and PC during the three strongest El Niño events for 1979–2016 are composited and centered at their peak in mid-December (i.e. month 12.5). Polynomials are fitted to the mean of these three events (Equations 2.6–2.8):

$$N34_{ideal.}(t) = -0.06 \cdot \omega(t)^6 + 0.07 \cdot \omega(t)^5 + 0.59 \cdot \omega(t)^4 - 0.29 \cdot \omega(t)^3 - 1.85 \cdot \omega(t)^2 - 0.03 \cdot \omega(t) + 1.77 \quad (2.6)$$

$$PC_{ideal.}(t) = 0.17 \cdot \omega(t)^9 + 0.13 \cdot \omega(t)^8 - 1.38 \cdot \omega(t)^7 - 0.93 \cdot \omega(t)^6 + 3.94 \cdot \omega(t)^5 + 2.19 \cdot \omega(t)^4 - 5.00 \cdot \omega(t)^3 - 2.09 \cdot \omega(t)^2 + 2.80 \cdot \omega(t) + 0.59 \quad (2.7)$$

with $\omega(t)$ centered and scaled:

$$\omega(t) = \frac{t - \mu}{s} \quad | \quad \mu = 12.5, s = 6.92, t = 1, \cdots, N \quad (2.8)$$

where μ is the location parameter identifying the peak of the event in mid-December of the first simulation year, s is the scale parameter indicating the spread of the polynomial function (wide vs. narrow) and t is the monthly time index for the two-year-long event. These polynomials are chosen as they best fit the data and start close to zero. The two polynomials are adjusted linearly at the beginning to ensure that later on, atmospheric perturbations increase/decrease from zero amplitude. In addition, the first part of the two time series is mirrored so that increase and decrease of atmospheric anomalies is identical (Figure 2.2a). To simulate symmetric events, the time series associated with La Niña are of negative amplitude with respect to the El Niño case (Figure 2.2b).

If instead composites of the three strong La Niña events (blue shaded time periods, Figure 2.1c) are used, the time series would show a reduced amplitude (dashed lines, Figure 2.2b). However, prescribing a symmetric atmospheric state for both events is advantageous in analysing the ocean's asymmetric response. The polynomials used to derive the time series for the La Niña composites are in Section A.2.

a) El Niño event b) La Niña event

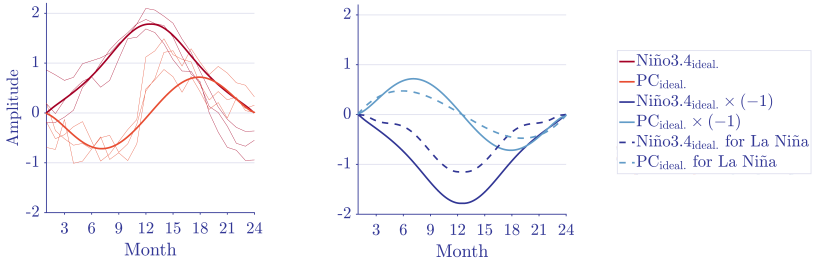

Figure 2.2: In a) the idealized symmetric time series for N34 and PC during El Niño is shown and in b) for La Niña spanning over two years. The solid lines represent the time series used in this study. The thin lines in a) show the observed Niño3.4 values (in dark red) and the calculated PC time series (in light red) during the three strongest El Niño events 1982–1983, 1997–1998 and 2014–2016. The dashed lines in b) represent the polynomial time series if composites of three strong La Niña events are used instead of the symmetric time series approach.

2.3.2 Idealized ENSO-related Regression Patterns

The regression analysis and the idealized time series provide the spatial evolution for the wind stress perturbations related to ENSO. The patterns of the remaining variables are obtained by regressing N34 and PC onto each anomaly field similar to Equation 2.2 resulting in two patterns for each input variable (Figures 2.3 and 2.4).

While the model is forced with wind speed, the wind stress patterns are shown here (Figure 2.3a,b and 2.4a,b). These patterns are used to derive the symmetric wind speed values for the model as will be discussed in Section 2.4.

a) Zonal wind stress

b) Meridional wind stress

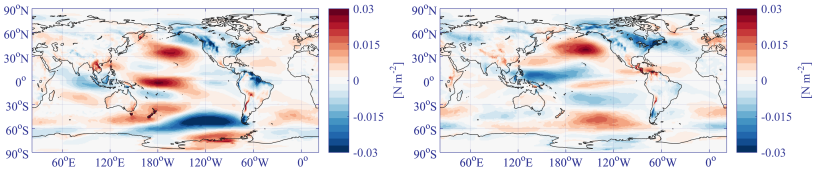

c) Air temperature

d) Specific humidity

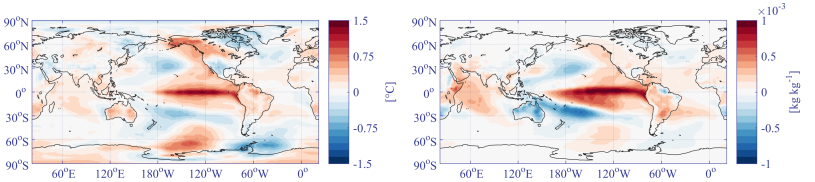

e) Downward long-wave radiation

f) Downward short-wave radiation

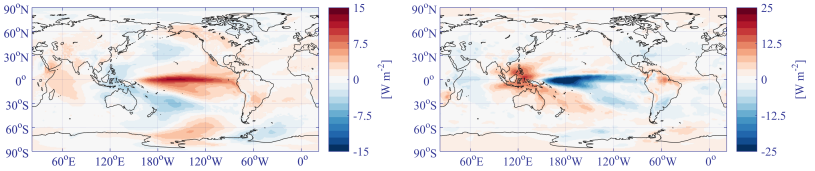

g) Precipitation

h) Sea level pressure

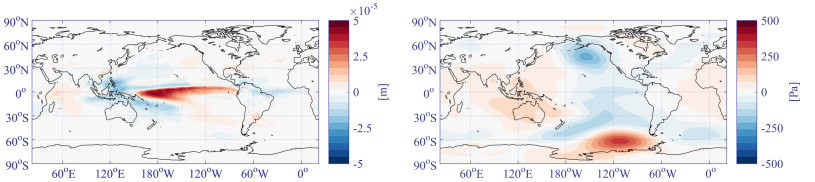

Figure 2.3: X_1 regression patterns of the eight atmospheric anomaly fields associated with the Niño3.4 index: a) Zonal wind stress [$\mathrm{N\,m^{-2}}$], b) meridional wind stress [$\mathrm{N\,m^{-2}}$], c) air temperature [°C], d) specific humidity [$\mathrm{kg\,kg^{-1}}$], e) downward long-wave radiation [$\mathrm{W\,m^{-2}}$], f) downward short-wave radiation [$\mathrm{W\,m^{-2}}$], g) precipitation [m] and h) sea level pressure [Pa]. In a) and b) the patterns for wind stress are shown as they are used to derive the correct wind speed values as will be discussed in Section 2.4).

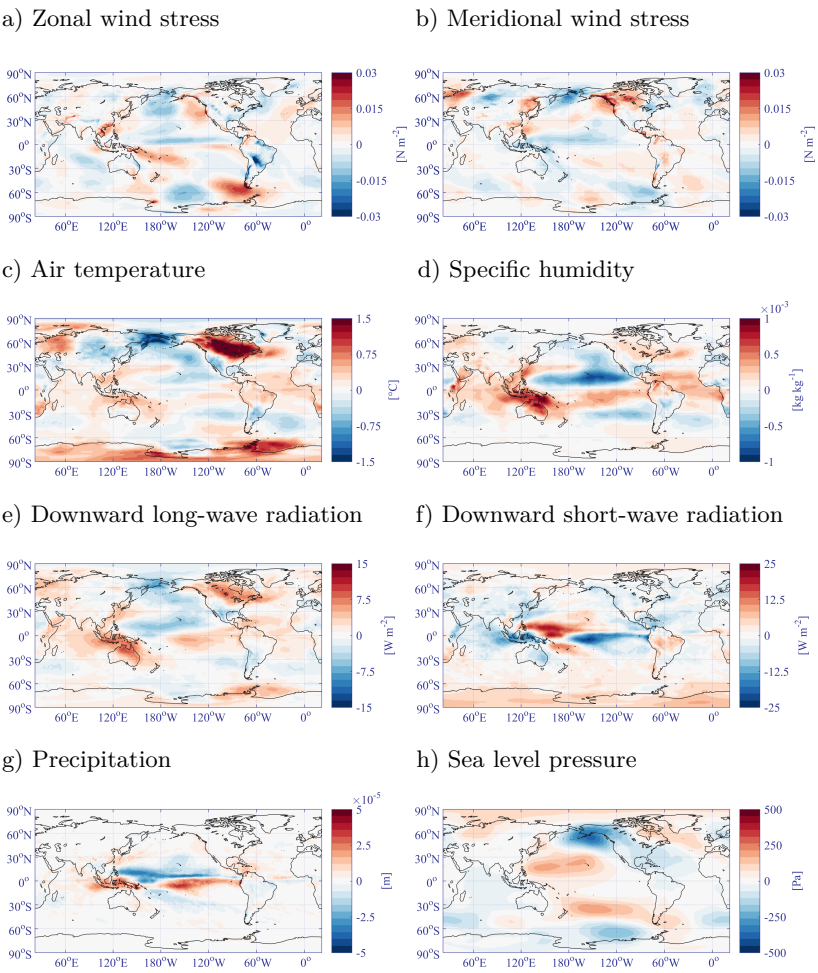

Figure 2.4: X_2 regression patterns of the eight atmospheric anomaly fields associated with the PC time series: a) Zonal wind stress [$\mathrm{N\,m^{-2}}$], b) meridional wind stress [$\mathrm{N\,m^{-2}}$], c) air temperature [°C], d) specific humidity [$\mathrm{kg\,kg^{-1}}$], e) downward long-wave radiation [$\mathrm{W\,m^{-2}}$], f) downward short-wave radiation [$\mathrm{W\,m^{-2}}$], g) precipitation [m] and h) sea level pressure [Pa]

The time evolution of all atmospheric forcing is calculated by multiplying the X_1 and X_2 patterns with their associated idealized time series and added to the climatological forcing (Equation 2.9).

$$F_{ideal.}(x,y,t) = \underbrace{\overline{F(x,y,t)}}_{climatology} + \underbrace{X_{1,F} \cdot N34_{ideal.} + X_{2,F} \cdot PC_{ideal.}}_{perturbation} \tag{2.9}$$

where $F_{ideal.}(x,y,t)$ is one of the eight idealized forcing anomaly fields dependent on time, $\overline{F(x,y,t)}$ is the base forcing field without any interannual variability from the CNYF dataset and $X_{1,F}$, $X_{2,F}$ are the regression patterns of a given field F.

2.4 Derivation of Surface Wind Speed

The model is forced with wind speed which is converted to wind stress using the wind stress law by Fairall et al. (1996):

$$\vec{\tau} = (\tau_x, \tau_y) = \rho_a \cdot C_D \cdot \underbrace{\sqrt{u_{10}^2 + v_{10}^2}}_{U_{10}} \cdot (u_{10}, v_{10}) \tag{2.10}$$

where ρ_a is the density of air ($1.25\ \mathrm{kg\,m^{-3}}$), C_D is the global-mean unitless drag coefficient (1.5×10^{-3}) according to Kara et al. (2007) and U_{10} is the wind speed magnitude .

However, as this experimental setup includes negative wind speed values (Figure 2.2b), the resulting stress is asymmetric due to the quadratic dependence of this formula on wind speed. To obtain a symmetric wind stress, the equation is solved for the two wind speed values u_{10} and v_{10} given the desired wind stress. The following part shows how this procedure is achieved:

First, the zonal component of the wind stress law is rewritten as a Reynold's decomposition:

$$\underbrace{\overline{\tau_x} + \tau_x'}_{l} = \underbrace{\rho_a \cdot C_D}_{k} \cdot \underbrace{\sqrt{(\overline{u_{10}} + u_{10}')^2 + (\overline{v_{10}} + v_{10}')^2}}_{U_{10}} \cdot (\overline{u_{10}} + u_{10}')$$

$$\Rightarrow l = k \cdot U_{10} \cdot (\overline{u_{10}} + u_{10}') \tag{2.11}$$

where $\overline{\tau_x}, \overline{u_{10}}$ and $\overline{v_{10}}$ are the climatological values, τ_x', u_{10}' and v_{10}' are the perturbation values, l is the total zonal wind stress forcing including climatological and perturbation values and k contains the two constants for the density of air and the drag coefficient.

Solving the second line of equation 2.11 for u_{10}' results in

$$u_{10}' = \frac{l}{k \cdot U_{10}} - \overline{u_{10}}. \tag{2.12}$$

The same procedure is applied to the meridional component and yields

$$m = k \cdot U_{10} \cdot (\overline{v_{10}} + v_{10}') \tag{2.13}$$

where m is the total meridional wind stress forcing including climatological and perturbation values. Solving equation 2.13 for v_{10}' results in

$$v_{10}' = \frac{m}{k \cdot U_{10}} - \overline{v_{10}}. \tag{2.14}$$

As a next step, the second line of equation 2.11 and equation 2.14 are combined resulting in the following expression:

$$l^2 + m^2 = k^2 \cdot U_{10}^2 \cdot [(\overline{u_{10}} + u_{10}')^2 + (\overline{v_{10}} + v_{10}')^2]$$
$$\Rightarrow l^2 + m^2 = k^2 \cdot U_{10}^4 \tag{2.15}$$

Equation 2.15 is solved for the positive magnitude U_{10}:

$$U_{10} = |\frac{\sqrt[4]{l^2 + m^2}}{\sqrt{k}}|. \tag{2.16}$$

Inserting equation 2.16 into equations 2.12 and 2.14 allows to solve for the two unknowns u_{10}' and v_{10}':

$$(u_{10}', v_{10}') = sign(\tau_x', \tau_v') \cdot \frac{(l, m) \cdot \sqrt{k}}{k \sqrt[4]{l^2 + m^2}} - (\overline{u_{10}}, \overline{v_{10}}) \tag{2.17}$$

The correct sign of equation 2.17 is determined using the wind stress anomaly spatial patterns.

A Note on Wind Speed Magnitude

By using this approach, it is ensured that the desired wind stress anomalies are applied to the model. However, wind speed values from Equation 2.17 are also used to calculate the wind speed magnitude in the bulk formulae of sensible and latent heat fluxes (Fairall et al. (1996), see Section A.3 for

the equations). Using the asymmetric wind speed values thus leads to asymmetric wind speed magnitudes and results in 18% higher mean wind speed deviation during La Niña than El Niño (Figure 2.5). While this asymmetry in wind speed magnitude is not ideal, it is of less importance than obtaining the correct symmetric wind stress values.

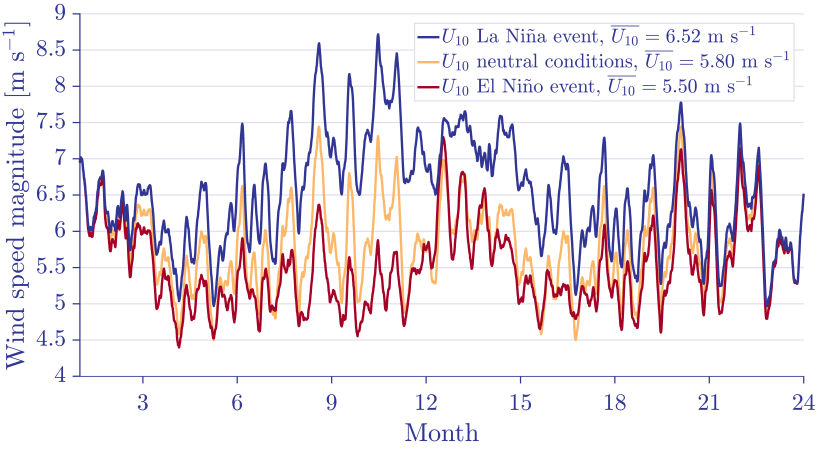

Figure 2.5: Mean wind speed magnitude over the region 5°S–5°N and 160°E–160°W for the strong El Niño and La Niña simulations as a 30–day moving average. The high variability within this data results from small-scale weather systems as it resembles the idealized atmospheric forcing with climatological and perturbation values combined.

2.5 Experimental Design

The following six experiments are run to evaluate the impact of ENSO events on the model's heat storage and WWV changes.

EXP_{EN}:	Simulation of a strong El Niño event over two years as a composite of three observed extreme events (1983–84, 1997–98 and 2014–16 followed by a spin-down period of two years with climatological forcing.
EXP_{LN}:	Simulation of a strong La Niña event as the inverse of EXP_{EN}'s atmospheric forcing followed by a spin-down period of two years with climatological forcing.
EXP_{EN+LN}:	Simulation of a full ENSO cycle consisting of a strong El Niño event, a subsequent strong La Niña event and a two year spin-down period.
EXP_{LN+EN}:	Same as in EXP_{EN+LN} but with reverse order of events.
$EXP_{mEN+mLN}$:	Simulation of a moderate ENSO cycle with 45% amplitude reduction in the two time series (i.e. with a maximum Niño3.4 = $\pm 1^{\circ}$C during El Niño/La Niña) followed by the two-year spin-down period.
$EXP_{mLN+mEN}$:	Same as in $EXP_{mEN+mLN}$ but with reverse order of events.

3

Results and Discussions

This chapter presents the simulated results organized in two parts. First, OHC asymmetries between El Niño and La Niña at the peak of the event are analysed as the respective anomalies show the highest magnitude. All anomalies in this study are calculated with respect to the mean of five unforced CNYF control simulations. Simulating full ENSO cycles with El Niño + La Niña as well as the reverse order of events reveals the asymmetry of the ocean's state after both cycles. The second part of the discussion focuses on the WWV balance throughout the ENSO cycle giving insight into the individual processes driving discharge and recharge during El Niño and La Niña.

3.1 Impact of ENSO on Ocean Heat Content

3.1.1 Response to El Niño and La Niña Events

As expected in the experimental setup, most anomalies are located in the tropical Pacific. During El Niño, a typical warm central and eastern Pacific develops and peaks in month 12 coinciding with the pre-defined westerly wind anomalies (Figures 3.1a, B.1a, ii). The Niño3.4 index reaches a maximum value of 1.57°C. This is approximately 12% lower than given by the idealized time series (Figure 2.2a) and is not unexpected as SST is dynamically determined by the ocean model.

The La Niña simulation during the same month exhibits a slightly different spatial SST pattern. While the warm central and eastern Pacific in the El Niño run extends from the South American coastline, most of the anomalous cold SST values are situated around 130°W in the La Niña case (Figures 3.1b and B.1b, ii).

a) Month 12 EXP_{EN}

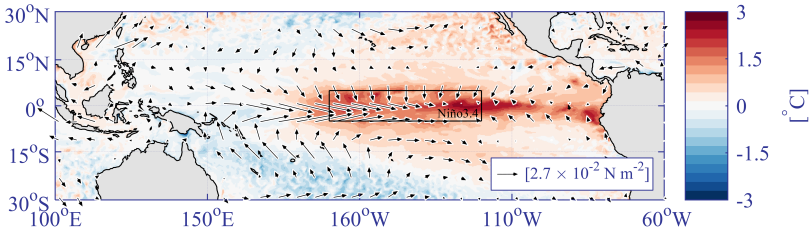

b) Month 12 EXP_{LN}

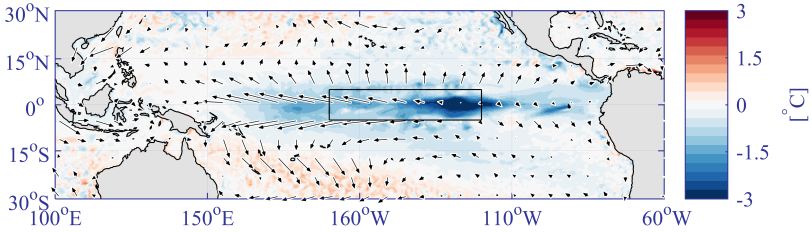

Figure 3.1: SST anomalies [°C] overlaid with wind stress deviations as arrows [10^{-2} N m^{-2}] at the peak of a) El Niño and b) La Niña. Wind stress anomalies are opposite for the two events as prescribed. The framed area represents the Niño3.4 region.

As discussed in Chapter 1, ENSO anomalies extend to the global scale. During the strong El Niño event in 1997–1998, the global mean sea surface temperature (GMSST) from the NOAA OI SST v2 dataset Reynolds et al. (2007) showed a maximum deviation of more than 0.2°C. In this study, the response in GMSST at month 12 is 0.09°C (Figure 3.2a). Strong wind stress anomalies as simulated with the global regression patterns $X_{1,\vec{\tau}}$ and $X_{2,\vec{\tau}}$ in the Southern Ocean between Australia and South America may reduce GMSST values by increasing upwelling of cold water masses.

The model's GMSST anomaly strongly correlates with the simulated Niño3.4 index ($r = 0.92$). In the last four months of the El Niño event (months 20–24), the Niño3.4 index is negative, indicating a cool surface despite the prescribed weaker trade winds (Figure B.1a, ii). This is a signal of the discharged state of the tropical Pacific.

When Niño3.4 is highest, the ocean's discharge of heat is strongest (large

negative OHC gradient, Figure 3.2a). In said figure, the OHC anomaly is shown as the identical globally integrated surface heating anomaly. Negative heat flux anomalies indicate that global ocean looses heat, particularly in water masses above 25°C (Figure B.2b). At month 12 of El Niño, warm water masses in the eastern tropical Pacific are exposed to the surface and loose heat either by transfer into the atmosphere, by meridional transport to higher latitudes or by vertical mixing into the ocean's interior (Lengaigne et al. (2012), Figure 3.2a). Heat fluxes from the ocean into the atmosphere are tightly correlated with Niño3.4 ($r = 0.72$) indicating that the warmest equatorial Pacific SST values coincide with the highest anomalous heat fluxes into the atmosphere (Johnson and Birnbaum, 2017). In this simulation, the surface heat flux into the atmosphere peaks one month before Niño3.4 (OHC and Niño3.4, Figure 3.2a, c). As this simulation has a higher temporal resolution compared to the study by Johnson and Birnbaum (2017), a one-month time lag is nearly identical to their findings.

The discharge phase, seen in the WWV anomalies (Figure 3.2c), lasts about one year, the same time duration as during the strong El Niño 1997–1998 (Meinen and McPhaden, 2000). WWV decrease is initiated at month 9 shortly before SST anomalies in the eastern Pacific are highest. Fourteen months later discharge ceases in the equatorial region and a subsequent recharge phase is initiated. The increase in WWV during months 20–24 may be occurring as the result of the strengthened Philippine anticyclone (Figure 2.1b) and the recovering trade wind strength. As the recently cooled water masses are once again exposed the surface, short-term heat uptake is facilitated as the temperature difference between atmosphere and ocean is enhanced.

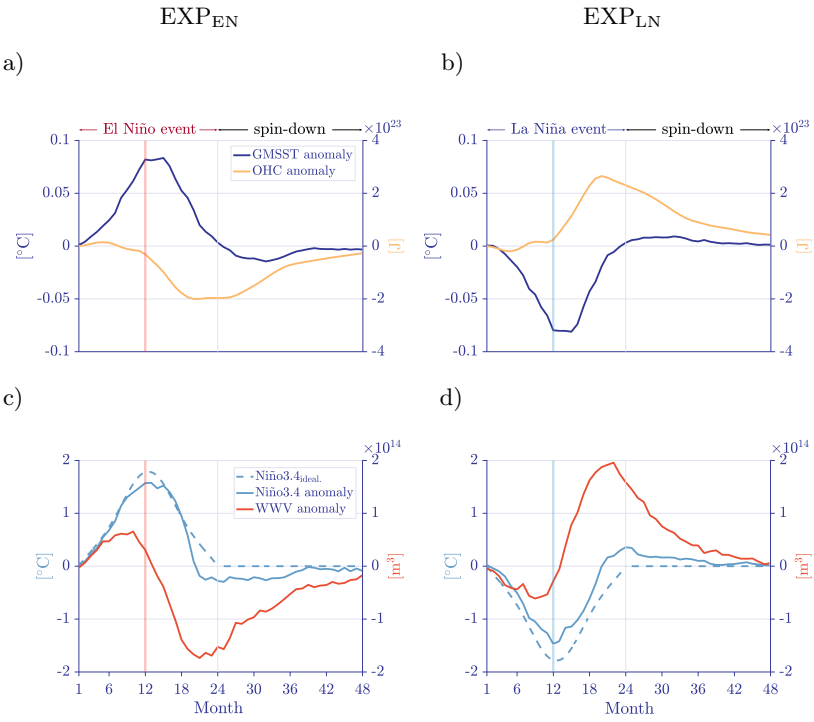

Figure 3.2: Time series of the strong El Niño and strong La Niña simulations followed by the two-year-long spin-down period. Figures a) and b) show GMSST [°C] and globally integrated OHC [J] anomalies while c) and d) show the idealized Niño3.4 (dashed line, same as in Figure 2.2), the simulated Niño3.4 index [°C] and WWV anomalies [m^3]. The vertical lines at month 12 indicate the peak of the specific event in December of the first simulation year. The vertical line at month 24 represents the end of the event and subsequent start of the spin-down period with climatological forcing.

WWV discharge during El Niño is restricted by its build-up prior to the event. The simulated WWV anomalies before the discharge phase are about 50% lower than during observed strong El Niño events with the same Niño3.4 index (Meinen and McPhaden, 2000). This is due to the El Niño event being initiated from climatological conditions with no prior WWV anomaly. This factor may contribute to the decreased strength of the simulated El Niño event relative to observations as WWV strongly influences the events' magnitude (Johnson and Lyman, 2014).

To first order, the anomalies in the La Niña simulation (3.2b, d) are opposite to the El Niño event. However, there are also considerable differences. OHC, while staying at a constant -2.5×10^{23}J over six months in the El Niño simulation, decreases during the same time period in the La Niña simulation (compare Figures 3.2a, b). This different signal during La Niña may be attributed to the ocean gaining more heat when equatorial Pacific SSTs are cool compared to its heat decrease during El Niño.

The spin-down periods in both simulations show that the ocean requires about as much time to equilibrate as the length of the previous event itself. GMSST and Niño3.4 adjust to neutral conditions faster than OHC and WWV due to the slower response of the ocean's interior relative to the surface.

Asymmetries in Temperature and Heat Response at Month 12

As shown in the two time series of GMSST and Niño3.4, the ocean's surface temperature response between El Niño and La Niña is strongest during the peak of both events. This section takes a closer look at the asymmetries between the events at this time.

The global horizontal average ocean temperature response at the peak of both El Niño and La Niña is restricted to the upper 750 m as it takes considerably longer than 12 months for signals to propagate deeper into the ocean's interior (Figure 3.3). As expected from the RDO theory and the observational study by Johnson and Birnbaum (2017), warming occurs in the upper ocean during El Niño (up to 0.13°C) and cooling during La Niña (up to −0.14°C). While the response to El Niño in the upper 100 m is about as strong as in the moderate (Niño3.4 = 1°C) event observed in Johnson and Lyman (2014), the mid-depth response is 2.5 times stronger in the simulations.

The mid-depth signal with cooling (warming) during El Niño (La Niña) is associated with the TC depth adjustment (Johnson and Birnbaum, 2017). During normal conditions, the TC is deep in the western and shallow in the eastern Pacific (Johnson and Birnbaum, 2017). This temperature response thus reveals that the TC depth anomaly in the West dominates the deep response and vice versa in the eastern Pacific (Figure B.1a, iii and Figure B.1b, iii). As a Hovmöller Diagram (i.e. a figure with longitude/latitude and time axes) only gives the equatorial mean response, the full spatial extent of the TC anomaly is clearer in depth-integrated OHC maps (Figure 3.4).

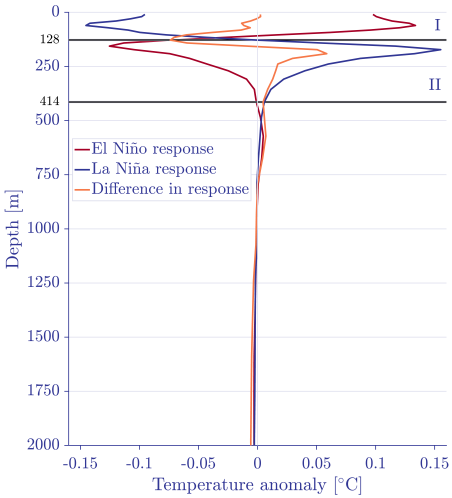

Figure 3.3: Global area-averaged ocean temperature response [°C] at the peak of the El Niño (red) and La Niña (blue) event (month 12). The orange line shows the difference in response. The horizontal lines at 128 m and 414 m depth denote the boundaries of the two depth levels I and II as in Johnson and Birnbaum (2017).

Heat content anomalies in the two depth layers I (surface-128 m depth) and II (128 m-414 m depth) are calculated from the temperature anomalies with

$$OHC(x, y, z, t) = \rho_0 \cdot c_p \cdot \int\int\int \Theta(x, y, z, t)\, dxdydz \tag{3.1}$$

where ρ_0 is the reference density of sea water (1035 kg m^{-3}), c_p is the specific heat capacity of sea water at constant pressure (3992.1 J kg^{-1} K^{-1}, Griffies (2012)), $\Theta = \Theta(S_A, \theta, p_0, t)$ is the conservative temperature [K] as a function of absolute Salinity S_A [g kg^{-1}], potential sea water temperature θ [°C], sea surface pressure p_0 (101325 Pa) and time t. Θ is calculated using the Thermodynamic Equation of Seawater 2010 toolbox (McDougall et al., 2009).

Both cooling and warming signals are close to symmetric in the uppermost layers (Figure 3.4a, b) and non-linear responses are more pronounced at depths between 128 m and 414 m. Anomalies in the WPWP during La Niña (Figure 3.4c) are stronger and more symmetric across hemispheres than in the El Niño simulation. In the Northern Hemisphere, the warm anomalies during La Niña (Figure 3.4c) extend through the Indonesian Throughflow (ITF) into the eastern Indian Ocean as the ITF is enhanced due to the increased sea surface height (SSH) difference between the Pacific Ocean and the Indian Ocean (Meyers, 1996; Liu et al., 2015).

Indian Ocean heat anomalies in both depth layers are highest along an elongated band at 8°S and may be caused by changes in the South Equatorial Current (Lumpkin and Johnson, 2013) or related to variations in the ITF (Sprintall et al., 2014).

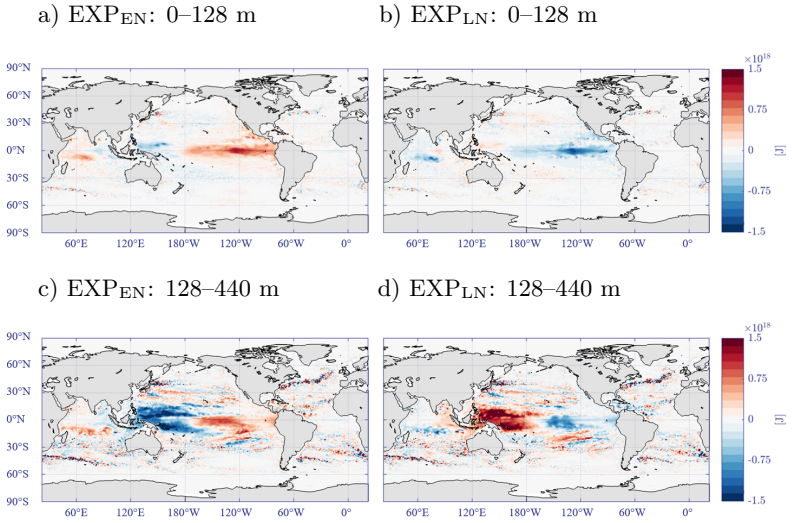

Figure 3.4: Depth-integrated ocean heat content response [J] to strong El Niño and La Niña events in the model at month 12 of the simulations for the two depth levels I and II defined in Figure 3.3 and similar as in Johnson and Birnbaum (2017).

While the depth-integrated heat content maps show near symmetric anomalies, there are two depth levels where the ocean's asymmetric response is strongest (Figure 3.3, orange line). At 128m depth, the temperature response to El Niño is stronger than to La Niña throughout the global ocean. More intense cooling than heating in the western and vice versa in the eastern Pacific drives the global response (Figure 3.5a, c). On the other hand, at 191m depth, the ocean's temperature response to La Niña in the WPWP is almost twice as large than to El Niño (+0.13°C vs. –0.07°C, Figure 3.3b, c). These strong signals originate in an increase of the temperature gradient across the climatological TC due to warming (cooling) above relative to the constant temperature of water masses below.

a) 128m depth b) 191m depth

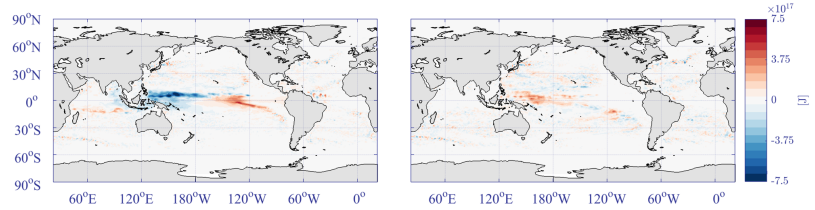

c) Sum of a) and b)

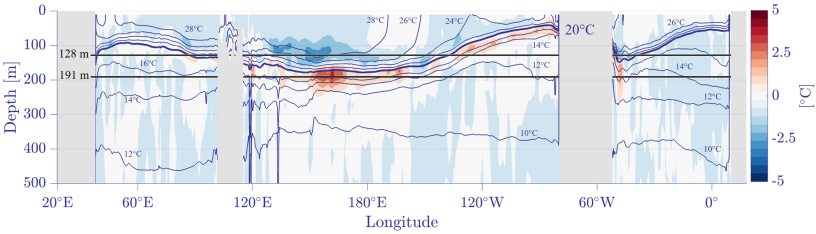

Figure 3.5: Map of OHC differences between the simulated a) El Niño and b) La Niña events at month 12 of the simulations [J]. In c) the longitude vs. depth section of the temperature anomaly difference averaged between 5°N and 5°S [°C]. Mean temperature contours [°C] in c) are overlaid with the TC in bold. Positive values indicate La Niña heats more than El Niño cools and vice versa.

The analysis thus far shows how temperature and ocean heat content responds to isolated ENSO events. However, most often these evens occur sequentially as is examined in the next Section.

3.1.2 Response During the Full ENSO Cycle

This section gives an overview of the anomalies during full ENSO cycles as well as the state of the ocean after a four-year-long oscillation.

As the ocean is not in a state of equilibrium after the first event, the residual anomalies impact the subsequent event. This effect is most clear in the OHC time series which shows that the total heat uptake for La Niña is increased by about 27% if it follows El Niño as compared to an isolated event (months 24–48, Figure 3.6a vs. months 1–24, Figure 3.2b). This is mainly

the result of heat being discharged during El Niño and the cooler ocean being able to take up considerable heat from the atmosphere. However, heat uptake in these simulations is directly linked to the strength of the trade winds as it ceases once the winds return to their climatological values (Figure 3.6a). On the other hand, heat release is also increased (+28%) if El Niño follows La Niña (months 24–48, Figure 3.6b vs. months 1–24 Figure 3.2a). This asymmetry in heat uptake and release also leads to the ocean requiring a longer time period to return to climatological conditions.

Asymmetries are also evident in the Niño3.4 index: If La Niña follows an El Niño, the Niño3.4 anomaly at the peak of the event is increased by ∼15% compared to a La Niña event in isolation (Figure 3.6c vs. months 1–24 Figure 3.2d)). This is due to the ocean being in a discharged state after the El Niño, reinforcing incipient changes in the Walker circulation.

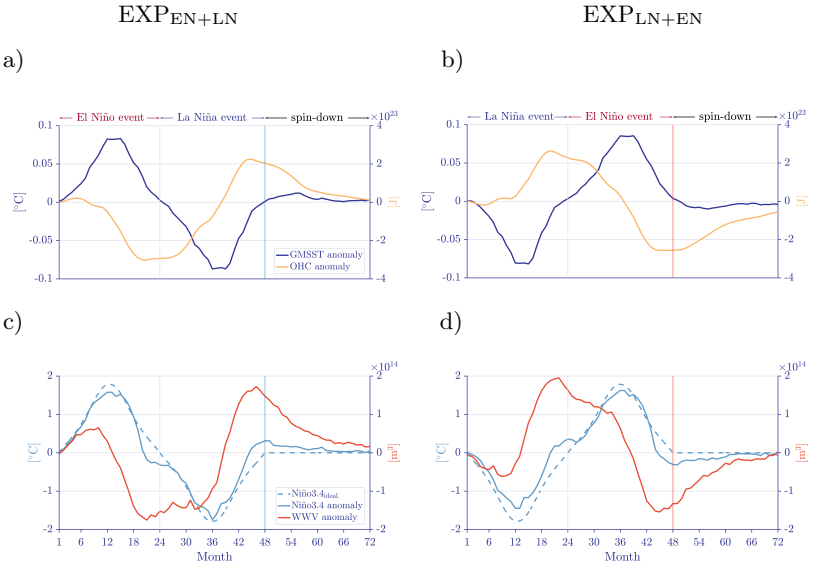

Figure 3.6: Time series of the strong ENSO cycle simulations with El Niño + La Niña and the reverse order of events followed by the two-year-long spin-down period. Figures a) and b) show GMSST [°C] and globally integrated OHC [J] anomalies while c) and d) show the idealized Niño3.4 (dashed line, same as in Figure 2.2), the simulated Niño3.4 index [°C] and WWV anomalies [m^3]. The vertical line at month 48 represents the end of the event and subsequent start of the spin-down period with climatological forcing.

Asymmetries in Temperature and Heat Response at Month 48

The ocean at the end of an ENSO cycle has not yet returned to neutral conditions. Residual equatorial temperature anomalies show that cooling (warming) is dominant in 150m depth in the western Pacific. While warming is stronger below the climatological TC if La Niña follows El Niño, cooling dominates above if the order of events is reversed (Figures 3.7a,b). Compared to the signal during peak of El Niño and La Niña, the residual signal extends further east as a result of the basin-wide recharged/discharged state of the ocean McGregor et al. (2014). As expected from the analysis in Section 3.1.1, asymmetries between the two ENSO cycles are located on either side of the climatological TC as a result of the vertical motion of the TC (Figure 3.7c).

Residual OHC anomalies are more pronounced in the Northern Hemisphere in the Pacific and Southern Hemisphere in the Indian Ocean (Figure 3.8a, b). In the Pacific, these anomalies are caused by the hemispherically asymmetric discharge and recharge of warm water masses during El Niño and La Niña respectively (McGregor et al., 2014). This effect will later on be discussed in Section 3.2. The Southern Hemisphere Indian Ocean signal is influenced by atmospheric teleconnections to the Pacific embedded in the regression patterns (Figures 2.3, 2.4) and the ITF. The residual anomalies in an elongated band at 8°S may be associated with a positive Indian Ocean Dipole (IOD) which often co-occurs with El Niño (Saji et al., 2017). Positive IOD events feature anomalous cooling off the coast of Sumatra/Java and warming in the western Indian Ocean (Yang et al., 2015). The residual Indian Ocean anomalies are mainly restricted to the Southern Hemisphere agreeing well with Rao and Behera (2005).

Asymmetries in OHC after the two ENSO cycles (Figure 3.8a, b) are generally small with a slightly stronger cooling anomaly at 10°N if El Niño occurs second (Figure B.3). This spatial pattern may, as mentioned above, be caused by the hemispherically asymmetric meridional transport during El Niño.

a) Month 48 $\mathrm{EXP}_{\mathrm{EN+LN}}$

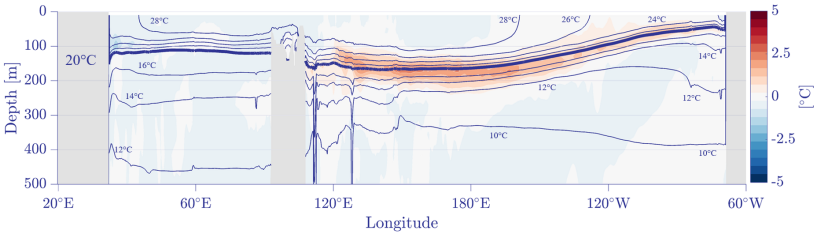

b) Month 48 $\mathrm{EXP}_{\mathrm{LN+EN}}$

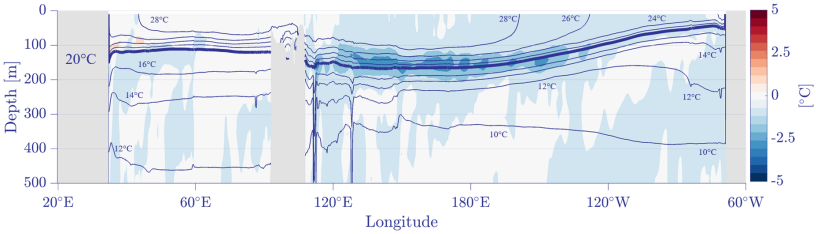

c) Sum of a) and b)

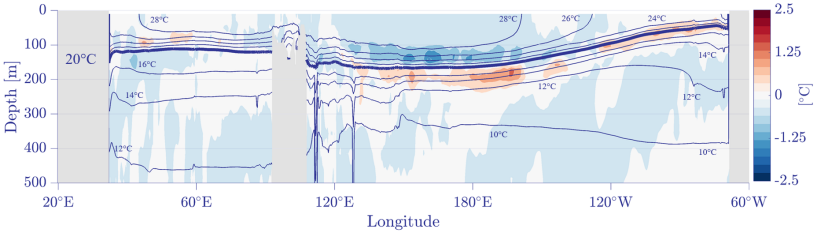

Figure 3.7: In a) and b) longitude vs. depth sections of temperature anomalies averaged between 5°N and 5°S at the end of the two ENSO cycles [°C]. In c) the sum of a) an b) with adjusted range of $[-2.5, 2.5]$°C for a clearer signal. Overlaid are contours of the climatological temperature.

Among others, meridional transport is a key component driving the discharge and recharge phases of ENSO. The next chapter will first give a short introduction into the different mechanisms that contribute to changes in the WWV over the seasonal cycle before investigating how the associated volume fluxes vary during El Niño and La Niña.

a) Month 48 EXP_{EN+LN}

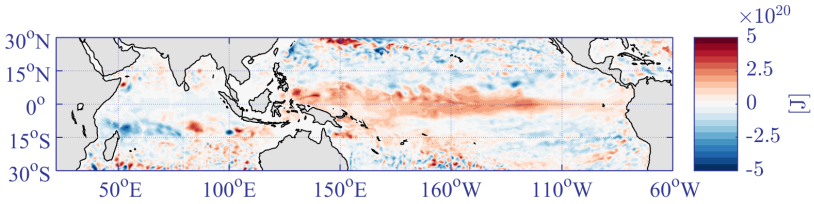

b) Month 48 EXP_{LN+EN}

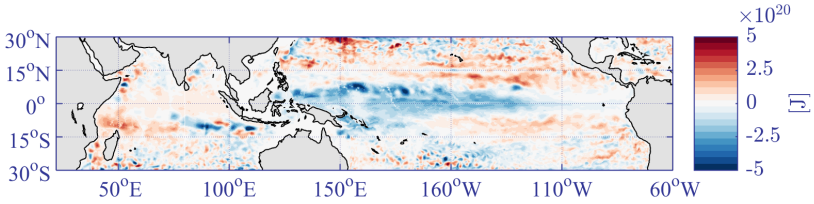

Figure 3.8: In a) and b) depth integrated OHC anomalies [J] at the end of the two ENSO cycles.

3.2 The Warm Water Volume Balance

WWV is not only a good indicator of equatorial OHC but also a key predictor in ENSO forecasts as it leads Niño3.4 values by 6–8 months (Bosc and Delcroix, 2008; McPhaden, 2012). This section will first give a brief theoretical introduction into the WWV balance before presenting its annual cycle and the anomalies throughout the ENSO cycle. To investigate the influence of individual vertical volume fluxes, the Water Mass Transformation (WMT) framework by Walin (1982) and improved by Iudicone et al. (2008) is used. WMT describes the processes which lead to a given water parcel's change in temperature and volume which is affected by both adiabatic and diabatic

processes.

The WWV balance is calculated in the region 5°N–5°S and 116°30'E–78°W with the ITF defined between East Kalimantan (116°30'E) and New Guinea (133°45'E) at 2°S (Figure 3.9). This region is also used in studies by Meinen and McPhaden (2000); Lengaigne et al. (2012); McGregor et al. (2014).

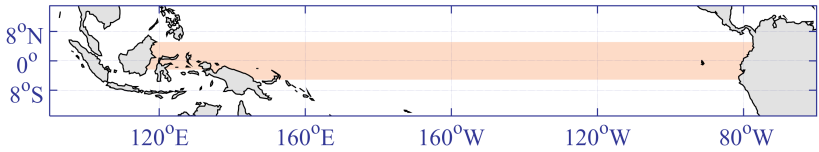

Figure 3.9: The WWV region between 5°N and 5°S framed by the coastlines of Borneo, South America and Papua New Guinea. The Indonesian Throughflow (ITF) is defined as the transect between East Kalimantan (116°30'E) through Sulawesi to New Guinea (133°45'E) at 2°S.

$$\frac{d(WWV)}{dt} = \underbrace{V(x,y,\Theta,t) + \mathcal{J}}_{Adiabatic\ Processes} + \underbrace{\mathcal{G}_{\mathcal{F}} + \mathcal{G}_{\mathcal{M}} + \mathcal{G}_{\mathcal{I}}}_{Diabatic\ Processes}$$
$$with\ \ \mathcal{G}_{\mathcal{F}} = \frac{\mathcal{F} \cdot a}{\rho_0 \cdot c_p \cdot \Delta T},\ \mathcal{G}_{\mathcal{M}} = \frac{\mathcal{M} \cdot a}{\rho_0 \cdot c_p \cdot \Delta T} \quad (3.2)$$

where $d(WWV)/dt$ is the change in WWV [$m^3\,s^{-1}$], $V(x,y,\Theta,t)$ is the meridional transport of water across y = (5°N, 5°S and the ITF) [$m^3\,s^{-1}$], $\mathcal{J}$ is the surface volume flux [$m^3\,s^{-1}$], $\mathcal{G}_{\mathcal{F}}$, $\mathcal{G}_{\mathcal{M}}$ are the vertical surface forcing and mixing volume fluxes across the TC [$m^3\,s^{-1}$], $\mathcal{G}_{\mathcal{I}}$ is the implicit volume flux calculated as the residual [$m^3\,s^{-1}$], $\mathcal{F}$ and $\mathcal{M}$ are the heat fluxes corresponding to $\mathcal{G}_{\mathcal{F}}$ and $\mathcal{G}_{\mathcal{M}}$ [$W\,m^{-2}$], a is the total area within the WWV region (2.04×10^{13} m^2) and $\Delta\Theta$ is the difference between two temperature bins in the water mass transformation diagnostics (0.5°C).

Adiabatic processes include the horizontal and vertical transport of heat by volume fluxes where the heat content of a given parcel is constant ($\Delta Q = 0$). Meridional transport through the transects 5°S, 5°N and the ITF as well as the vertical surface volume flux $\mathcal{J}$ by precipitation, evaporation and river run-off are both adiabatic processes (Figure 3.10).

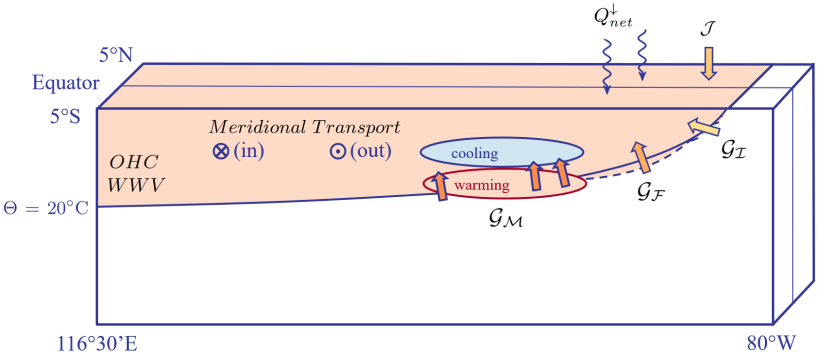

Figure 3.10: Simplified box model of volume fluxes influencing WWV in the equatorial Pacific above the thermocline. OHC and WWV denote the quantity above the TC (shaded volume). Meridional transport moves volume into and out of the region. $\mathcal{G}$ is the surface volume flux and $\mathcal{G}_{\mathcal{M}}$ the vertical mixing volume flux across the TC from warmer (red shaded area) to cooler (blue shaded area) water. $\mathcal{G}_{\mathcal{F}}$ is the surface forcing volume flux due to the downward net surface heat flux ${Q_{net}}^{\downarrow}$ and $\mathcal{G}_{\mathcal{I}}$ indicates implicit mixing. To simplify the schematic, the arrows only show fluxes into the WWV region.

The diabatic processes represent vertical heat fluxes warming or cooling WWV and thus increasing and decreasing its volume ($\Delta Q \neq 0$). The downward net surface heat flux warms ocean water masses at the surface and in the upper-most layers (Equation 3.3).

$$Q_{net}^{\downarrow} = F_{SW}^{\downarrow} + F_{LW}^{\downarrow} + SH + \lambda E \tag{3.3}$$

where $Q_{net}^{\downarrow}$ is the downward net surface heat flux [W m^{-2}], $F_{SW}^{\downarrow}$ is the downward short-wave heat flux, $F_{LW}^{\downarrow}$ is the downward long-wave heat flux, SH is the sensible heat flux and λE is the latent heat flux all in units of [W m^{-2}]. Through surface heating, water moves to warmer temperature regions resulting in a volume flux across the TC ($\mathcal{G}_{\mathcal{F}}$, Figure 3.10). Diffuse vertical mixing (and the non-local heat flux within the KPP boundary layer scheme of Large et al. (1994)) also lead to diabatic temperature changes as it cools near the surface and warms deeper water masses resulting in a temperature and subsequent volume exchange (shaded areas, Figure 3.10). The associated climatological volume flux of the rising warm water masses across the TC is thus directed into the WWV region ($\mathcal{G}_{\mathcal{M}}$, Figure 3.10).

Implicit mixing is an additional mixing process associated with truncation errors in the advection scheme that result from optimizing numerical calculations. As the model does not include horizontal diffusion, the advection scheme smooths strong horizontal gradients (the implicit mixing) representing horizontal mixing near the grid cell border. However, as the advection scheme is three-dimensional, implicit mixing may also include small parts of vertical mixing. This term is calculated as the residual ($\mathcal{G}_{\mathcal{I}}$, Figure 3.10). See Holmes et al. (2018) for more information.

The two WMT fluxes as well as $\mathcal{J}$ are calculated separately at each spatial location and time step during the simulation (i.e. they are diagnostic variables and follow the procedure discussed in Holmes et al. (2018).

3.2.1 The Climatological WWV Balance

In order to understand the WWV-associated fluxes throughout the ENSO cycle, the seasonal cycle is investigated first. The model's climatological WWV exhibits, consistent with observations by Meinen and McPhaden (2000), an interannual variability of $3 \times 10^{14}\mathrm{m}^3$ (i.e. time-integral of the change in WWV, Figure 3.11). The annual mean balance is approximated between the adiabatic and diabatic fluxes resulting in an annual mean change in WWV of 0.56Sv. This small positive value may be a small residual error in the temperature bin calculations of the model. It is much smaller than the other balance terms and the changes throughout the annual and ENSO cycles.

Upwelling of cold water masses in the eastern equatorial Pacific leads to an annual mean WWV addition by surface forcing (+2.7 Sv, 1 Sv $= 10^6$ m^6 s^{-1}), vertical mixing (+6.8 Sv) and implicit mixing (+3.5 Sv). The increased WWV is balanced by meridional transport across 5°N and 5°S (−6.5 Sv) as well as flow through the ITF (−6.1 Sv). The impact of surface volume fluxes as suggested in Meinen and McPhaden (2001); Lengaigne et al. (2012) is negligible compared to the other terms and will not be discussed further.

WWV depletes in the first half of the year as meridional transport across 5°N, 5°S and in particular the ITF move warm water masses out of the WWV region (Figure 3.11). The diabatic vertical mixing and surface forcing volume fluxes are both small during the first six months. In the second half of the year, trade winds shift southward and intensify, increasing both WWV build-up and depletion by an increased Ekman flow across 5°N and 5°S (Wyrtki and Meyers, 1976). The vertical mixing heat flux is more dominant than

the surface forcing heat flux in WWV build-up during austral winter and spring. The high rates of vertical mixing are caused by the shallower TC and increased turbulence as trade winds increase (Liu et al., 2016). Both diabatic heat fluxes are stronger than the increase in Ekman transport leading to a net increase in WWV starting in August.

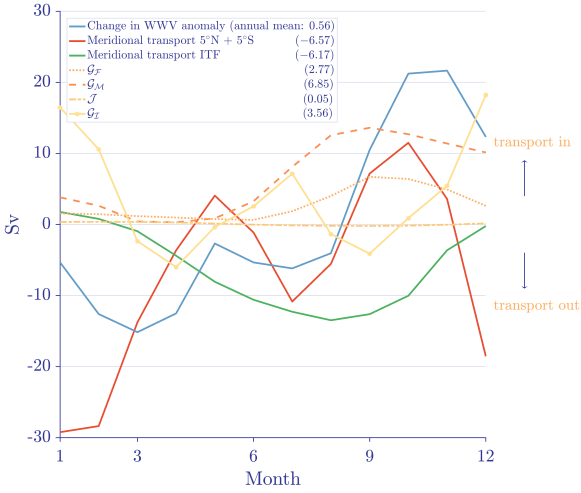

Figure 3.11: Annual cycle of the climatological WWV balance terms [Sv]. Positive values indicate a volume flux into the region. A 3–month running mean has been applied.

3.2.2 The WWV Balance Throughout the ENSO Cycle

Over the ENSO cycle, WWV undergoes changes associated with recharge and discharge periods which will be the focus of the analysis here. The discharge phase during El Niño is defined as the period when the change in WWV anomaly is negative (blue area from month 9–22, Figure 3.12a). To ensure a symmetric analysis, the recharge phase during La Niña covers the same time period two years later (blue area, Figure 3.12a) and the two phases are reversed for the simulation with La Niña + El Niño (blue and red regions, Figure 3.12b).

a) $\mathrm{EXP}_{\mathrm{EN+LN}}$

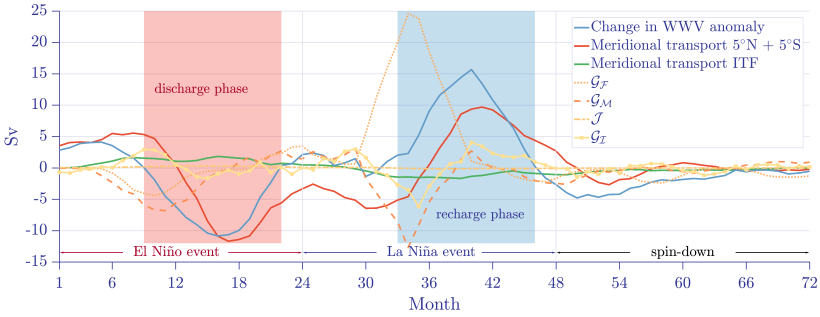

b) $\mathrm{EXP}_{\mathrm{LN+EN}}$

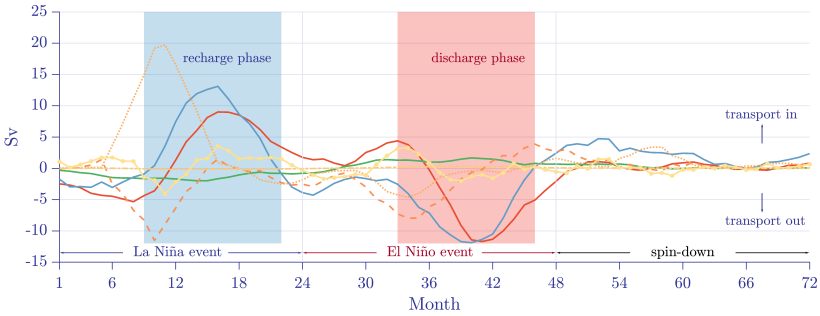

Figure 3.12: The various WWV balance terms [Sv] as anomalies throughout the ENSO cycle calculated in the region outlined in Figure 3.9. In a) the oscillation with El Niño followed by La Niña and in b) the ENSO cycle with a reverse order of events. A five month running mean as in Meinen and McPhaden (2000) has been applied. The discharge phase (red region in a) is defined as the time period when the change in WWV is negative from months 9–22 and the recharge period covering the same months is defined two years later (blue region). In b) discharge and recharge periods are exchanged. Positive (negative) values indicate a net transport into (out of) the WWV region as indicated on the right hand side in b). The vertical lines at month 24 and 48 indicate the end of the first and second event of the oscillation.

El Niño Discharge

The discharge phase during El Niño is initiated at month 9 when the change in WWV anomaly becomes negative (Figure 3.6a). WWV depletion thus starts three months ahead of the peak of El Niño and leads over the 14 month period to a total volume decrease of 2.25×10^{14} m^3 (Table 3.1). Depletion of WWV occurs in two steps with an initial decrease driven mainly by vertical volume fluxes followed by meridional transport out of the region (red area, Figure 3.12a).

	$\mathbf{EXP_{EN+LN}}$		$\mathbf{EXP_{LN+EN}}$	
All units: $[\mathbf{10^{14}\ m^3}]$	**Discharge Phase**		**Recharge Phase**	
		Percentage		Percentage
Change in Warm Water Volume	−2.25	100%	+2.37	100%
Meridional transport 5°N + 5°S	−1.79	79.42%	+1.53	64.38%
Meridional transport ITF	+0.46	−20.68%	−0.51	−21.61%
Horizontal Volume Flux:	− 1.33	**58.74 %**	+ 1.02	**42.77 %**
$\mathcal{G}_{\mathcal{F}}$	−0.35	15.81%	+2.39	100.67%
$\mathcal{G}_{\mathcal{M}}$	−0.73	32.70%	−1.16	−48.87%
$\mathcal{G}_{\mathcal{J}}$	+0.08	−3.92%	−0.04	−2.00%
$\mathcal{G}_{\mathcal{I}}$	+0.07	−3.33%	+0.17	7.43%
Vertical Volume Flux:	− 0.93	**41.26 %**	+ 1.36	**57.23 %**

Table 3.1: Total contribution of each WWV balance term during the 14 month long discharge and recharge periods as defined in Figure 3.12. All values are time-integrated and in units of [10^{14} m^3]. Positive (negative) values indicating volume transport into (out of) the WWV region.

Surface forcing (dashed line) and the vertical mixing heat flux (dotted line, Figure 3.12a) drive the initial stage of WWV discharge. Compared to the seasonal cycle, vertical mixing is decreased during this early discharge period due to the weakening of the trade winds and the deeper TC (i.e. less turbulence) driving a negative anomalous volume flux out of the WWV region. The surface forcing volume flux is also weakened relative to normal conditions as warmer SST values are driving heat release to the atmosphere and therefore a negative anomalous volume flux across the TC results. These two diabatic processes combined lead to a net volume transport of 1.08×10^{14} m^3 across the TC out of the WWV region. The total vertical volume flux throughout the discharge phase amounts to a volume change of -0.93×10^{14} m^3 and contributes ∼40% (as in Lengaigne et al. (2012)) to the total WWV change.

The second stage of the discharge phase with meridional transport as the dominant driver occurs about six months later. During the initial discharge phase, meridional transport through 5°N and 5°S is opposing WWV depletion by moving anomalous warm waters into the region as wind stress anomalies are confined to the Northern Hemisphere (Figure 2.1a, b, McGregor et al. (2014)). This creates a large-scale southward Ekman flow into the WWV region (McGregor et al., 2014). With the shift in wind stress anomalies to the Southern Hemisphere during the second year of the simulation, the wind stress forcing induces a basin-wide northward flow out of the WWV region (McGregor et al., 2014) reducing the WWV.

While the large-scale horizontal transport through the two transects 5°N and 5°S during the second stage of discharge is high, the strength of the ITF is decreased throughout the full discharge phase (green line, Figure 3.12a). This is the result of the reduced SSH difference between the Indian and the Pacific Ocean (Sprintall and Révelard, 2014). Including the ITF, the total horizontal transport during the discharge period is contributing with $1.33 \times 10^{14}\mathrm{m}^3$ about 60% to the WWV changes (Table 3.1); identical to the value given in Lengaigne et al. (2012).

Implicit mixing (calculated as the residual) plays a minor role throughout the discharge phase contributing only 3% to the WWV changes. The highest rates of implicit mixing occur during the initial stage of discharge and counteract vertical mixing by diffusion of heat into the region. This process may be attributed to horizontal mixing across isotherms in the eastern equatorial Pacific (Holmes et al., 2018).

La Niña Recharge

As during El Niño, the change in warm water volume during La Niña occurs over two stages with an initial phase dominated by the diabatic fluxes and the latter half of the recharge phase mainly controlled by meridional transport. During La Niña's recharge, the total change in WWV is $2.73 \times 10^{14}\mathrm{m}^3$, about as high as the change in volume during El Niño's discharge phase (Table 3.1).

Compared to El Niño's discharge phase, not all volume fluxes are opposite and of the same magnitude. The most striking differences lie in the vertical mixing and surface forcing fluxes (red area, Figure 3.12b). The strengthened trade winds increase turbulence and vertical mixing in the upper-most layers of the ocean thus increasing mixing rates. However, the vertical mixing volume flux does not increase but decreases WWV. This is likely the result of the upward shift of the TC in the eastern equatorial Pacific being positioned

in a region where strong mixing cools water masses. The result is a strong vertical volume flux across the TC out of the WWV region (Figure 3.13b).

The surface forcing volume flux clearly dominates WWV build-up with a much stronger response compared to the discharge period. The increased trade wind strength, shallower TC (up to 40m; Figure B.1b, iii) and cold SST (up to $-2.5°C$; Figure B.1b, ii) values lead to high heat absorption in the eastern equatorial Pacific, thus warming the upper-most surface layers. This results in a strong volume flux across the TC into the WWV region (Figure 3.13b). The total contribution of the surface forcing volume flux to the WWV increase is $2.39 \times 10^{14} m^3$ (100.67%). However, as the vertical mixing contribution balances this large volume flux, the overall vertical volume transport is ∼57% (Table 3.1). This value is slightly lower than in Lengaigne et al. (2012) where diabatic processes contributed about 70% to the strong La Niña WWV build-up in 1984, 1988 and 1999. These two values do not disagree. Some discrepancies between the study here and Lengaigne et al. (2012) are expected due to the different experimental design.

Implicit mixing during the recharge phase of La Niña as during El Niño plays only a minor role (Figures 3.12a, b). It is responsible for just 3.5% to 7.5% of the changes in WWV. The strongest rates of implicit mixing during La Niña coincide with the peak in vertical mixing as this process is enhanced in regions with large horizontal and vertical velocity gradients. This occurs in the eastern equatorial Pacific with a strong circulation and many small-scale eddies.

a) El Niño discharge phase

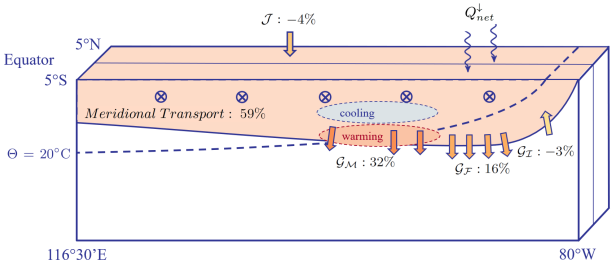

b) La Niña recharge phase

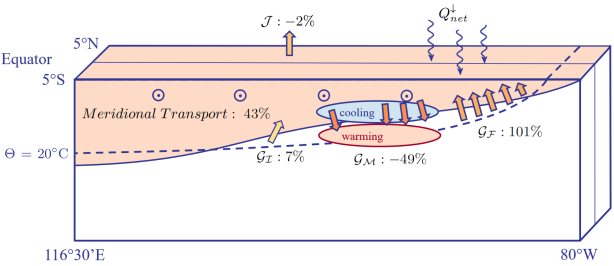

Figure 3.13: The various anomalous WWV balance terms during a) El Niño's discharge and b) La Niña's recharge phase. The dashed line is the climatological TC and the solid line in the side view the anomalous TC during the discharge and recharge phase. The shaded volume above the TC indicates the WWV. The blue (and red) shaded areas indicate vertical mixing cooling (warming) water masses. $Q_{net}{}^{\downarrow}$ is the downward net surface heat flux and $\mathcal{G}_{\mathcal{F}}$, $\mathcal{G}_{\mathcal{M}}$, $\mathcal{G}_{\mathcal{I}}$ and $\mathcal{J}$ are the surface forcing, vertical mixing, implicit mixing and surface volume fluxes. The blue shaded area in b) denotes where vertical mixing cools water masses. The percentage values show the contribution of each volume flux to the total discharge and recharge or warm waters.

Contrary to the vertical fluxes, meridional transport into the WWV region during the recharge phase is largely symmetric to the discharge of El Niño. As during discharge, horizontal transport lags changes in WWV by three months as the southward shift in wind anomalies to the Southern Hemisphere is required for driving most of the anomalous horizontal transport. Contrary to the meridional transport across 5°N and 5°S, the ITF is consistently increased throughout the full discharge period (blue area, Figure 3.12b). The strong trade winds continuously increase the SSH in the western equatorial Pacific resulting in the increased ITF values and subsequent WWV transport out of the region. In total, the meridional transport is re-

sponsible for approximately 45% of the total recharge as compared to the ∼60% contribution during El Niño's discharge (Table 3.1).

Asymmetries between the La Niña event occurring first or second in an ENSO cycle are generally small with only minor differences in the total WWV balance terms (red areas, Figure 3.12a, b). As expected, the total recharge increases by about 10% if La Niña follows El Niño (Table 3.1, B.1). The same finding applies to El Niño's discharge period which is enhanced by about 13% if it follows La Niña. As mentioned above in Section 3.1.2 it is the result of residual anomalies impacting the subsequent event.

3.3 Moderate Events

This study's focus has been on extreme events as the asymmetries typically increase with magnitude of the events (Levine et al., 2016). However, nonlinearities between El Niño and La Niña are also apparent in moderate events. The moderate simulations show that overall asymmetries are reduced when the amplitude is reduced. This is particularly visible in the OHC and WWV anomaly time series (Figure 3.14) compared to the time series shown above (Figure 3.6).

The reduction of approximately 45% in the atmospheric anomalies also results in an almost equivalent reduction of total WWV changes during discharge and recharge periods (Table 3.1, B.1). Correspondingly, the adiabatic and diabatic volume fluxes are also decreased in a similar manner. The strong asymmetries between the vertical heat fluxes during discharge and recharge phases also occur during moderate events with the surface forcing volume flux contributing about as much to the total WWV change as in an extreme event (Table B.2). Overall, the moderate events confirm that the mechanisms driving heat uptake and WWV variability during extreme ENSO events are also apparent.

Furthermore, the moderate La Niña here (i.e. a 45% reduction of the idealized time series amplitude) is much closer to a real observed La Niña when comparing the solid and dashed lines in Figure 2.2b).

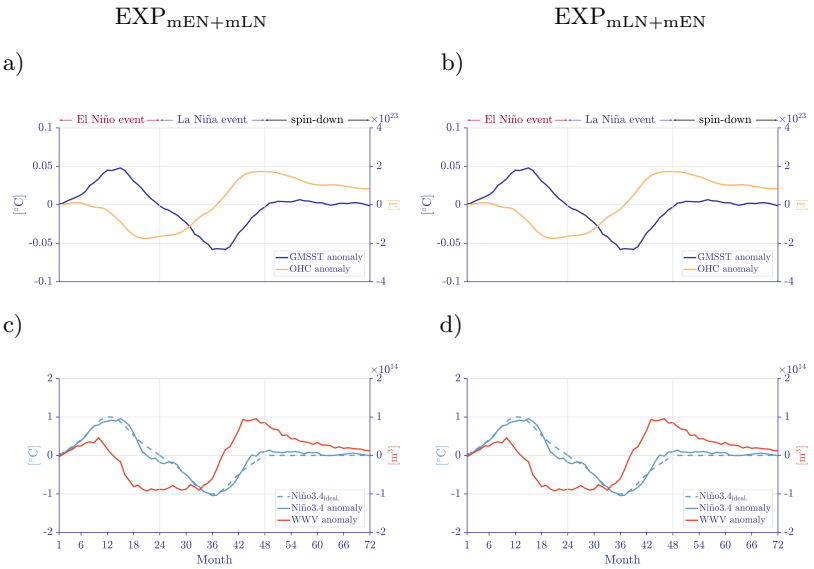

Figure 3.14: Time series of the moderate ENSO cycle simulations with El Niño + La Niña and the reverse order of events followed by the two-year-long spin-down period. Figures a) and b) show GMSST [°C] and globally integrated OHC [J] anomalies while c) and d) show the idealized Niño3.4 (dashed line, same as in Figure 2.2), the simulated Niño3.4 index [°C] and WWV anomalies [m^3].

3.4 A Note on the Ensemble Approach

To increase the signal-to-noise ratio, five ensemble runs with slightly different initial conditions have been simulated (see Appendix C on how the ensemble runs were set up). The simulations show that variability within the control ensemble is much weaker than the forced variability (Figure 3.15). Therefore the ensemble approach has not been further continued.

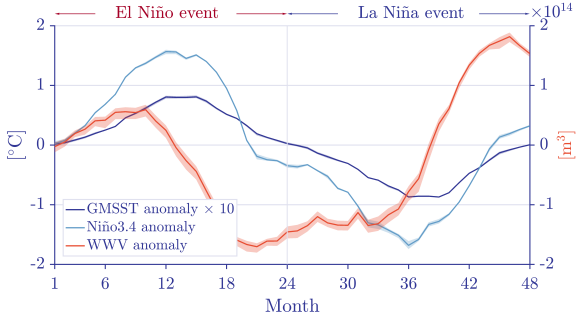

Figure 3.15: Time series of GMSST [1/10°C], Niño3.4 [°C] and WWV [m]from the EXP_{EN+LN} simulation with five ensembles each varying slightly in its initial conditions. The GMSST anomaly time series has been multiplied by 10 for a clearer signal. The shaded area indicates the difference between the highest and lowest value within the ensembles with the solid line representing the ensemble mean.

4

Conclusions and Outlook

The primary goal of this study was to simulate idealized symmetric El Niño and La Niña events to assess non-linear ocean responses to these atmospheric perturbations, particularly in regard to ocean heat content and warm water volume anomalies. The RDO theory assumes that the ocean response should be the opposite between the two events, but it was shown that this is not the case. Non-linear behaviour arising from the dependence of the surface heat fluxes on SST, from the Indonesian Throughflow and from vertical heat fluxes each contribute to a complex interplay resulting in different states of the ocean once conditions return to normal.

It was shown in Chapter 3 that the ocean's response to the La Niña-type forcing was stronger than to El Niño-type forcing with regards to the global mean ocean temperature, ocean heat content and warm water volume. In short, the ocean warms more during La Niña than it cools during El Niño. However, the simulations conducted here differ from observed events where the Niño3.4 index is generally weaker for La Niña and thus an observed ENSO cycle does not necessarily lead to net heat uptake by the ocean.

For the first time, use of the water mass transformation framework made it possible to examine the timing, magnitude and contribution of different diabatic processes to variations in warm water volume during a full ENSO cycle. Establishing the warm water volume balance in the equatorial region 5°N–5°S revealed a two-stage warm water volume change during El Niño's discharge and La Niña's recharge phase: The initial phase was dominated by the surface forcing and vertical mixing volume fluxes which show a strong asymmetry between El Niño and La Niña. The strength of the trade winds, the temperature of the sea surface, the intensity of turbulence in the uppermost layers of the ocean as well as the position of the thermocline were described as key mechanisms to determine the contribution of the diabatic fluxes to the total volume change. The second stage during discharge and recharge, occurring three months later, was controlled by meridional trans-

port across 5°N and 5°S with the ITF opposing the volume flux through the two transects. The onset of strong meridional transport is linked to the southward wind shift across hemispheres leading to basin-wide Ekman transport (McGregor et al., 2014).

The increased influence of the diabatic terms during La Niña is in particular important in the context of current climate change. With the ocean absorbing more than 90% of the additional anthropogenic heat (Johnson and Lyman, 2014) and an increased probability of extreme ENSO events in the future (Collins et al., 2010; Cai et al., 2014, 2015), the eastern equatorial Pacific will be a key region in mixing additional heat into deeper layers of the ocean. This added heat may lead subsequently to sea-level rise by thermosteric expansion which would be detrimental to Small Pacific Island States that are located in this region.

4.1 Future Work

Composite La Niña Events:
The experimental setup was designed to isolate the ocean response to El Niño and La Niña in a theoretical framework. As observed La Niña events differ both in length and magnitude to the ones simulated in this study. Heat anomalies after the full ENSO cycle are not representative of real events. Therefore, it would be beneficial to simulate La Niña events with idealized time series from a composite of the three observed extreme events 1988-1990, 2007-2008 and 2010-2011 (dashed lines, Figure 2.2b). The polynomials for these time series are presented in the Appendix (Section A.2).

Non-mirrored Idealized Time Series:
The idealized time series for the second year of an El Niño and La Niña event were mirrored from the first year to ensure a symmetric increase and decrease of atmospheric anomalies throughout the event (Figure 2.2). With this design choice, the peak of the PC time series was reduced. Including the second part of the polynomial time series in a future simulation could change the strength of the southward wind shift and therefore the related meridional transport across 5°N and 5°S.

Pacific-only Forcing:
As mentioned in Section 3.1, Indian Ocean heat anomalies arise due to the

co-occurrence of El Niño and a positive Indian Ocean Dipole. It would be valuable to consider a second set of experiments separating changes in the Pacific from changes in other regions by removing atmospheric teleconnections, i.e. by forcing anomalies only over the Pacific region (Figure 4.1).

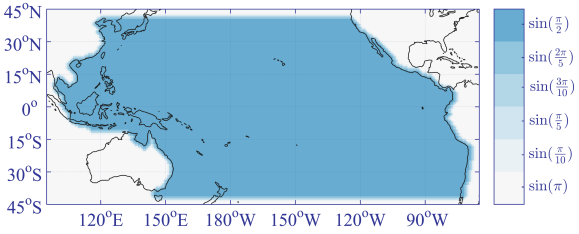

Figure 4.1: Proposed Pacific-only region mask where the input would be reduced over four grid points using the scaling factor $sin(x)$ with $x \in (\pi/2, \pi)$.

El Niño Modoki:
While extreme El Niño (La Niña) events such as the ones simulated in this study exhibit the typical warm (cold) sea surface temperature anomalies in the eastern Pacific, moderate events can be quite different. El Niño Modoki (も ど き, jpn: 'a similar but different thing') displays a peak warming of sea surface temperature in the central Pacific surrounded by cooler areas East and West (Ashok et al., 2007). Using the approach in this study to simulate El Niño Modoki would give valuable insight on how the processes that are influencing changes in warm water masses are driven by event type and magnitude.

A

Additional Calculations

A.1 Southern Oscillation Index

The SOI is calculated as the difference of standardized sea level pressure anomalies based on the 1981–2010 period at the two locations Tahiti (French Polynesia) and Darwin (Australia) divided by the monthly standard deviation Ropelewski and Jones (1987), Equations A.1–A.3)[1].

Standarized Index in Tahiti:

$$st.\,Tahiti(t) = \frac{SLP_T(t) - \overline{SLP}_T}{\sigma_T(t)}$$

$$\sigma_T(t) = \sqrt{\sum_{i=1}^{N} \frac{(SLP_{i,T}(t) - \overline{SLP_T})^2}{N}} \tag{A.1}$$

where SLP_T is a given sea level pressure value in Tahiti, $\overline{SLP}_T$ is the climatological value and σ_T is the standard deviation of SLP in Tahiti. The same procedure is applied to the values in Darwin. The monthly standard deviation is calculated as:

$$MSD(t) = \sqrt{\sum_{t=1}^{N} \frac{(st.\,Tahiti - st.\,Darwin^2}{N}} \tag{A.2}$$

and the SOI is given by

$$SOI(t) = \frac{st.\,Tahiti - st.\,Darwin}{MSD} \tag{A.3}$$

[1] http://www.cpc.ncep.noaa.gov/data/indices/Readme.index.shtml.

A.2 Polynomials for a Composite of La Niña Events

If a composite of three strong La Niña events were chosen to obtain the idealized $N34$ and PC time series, different polynomials would have been used (Equations A.4 and A.5).

$$Niño3.4(t) = -0.02 \cdot \omega(t)^7 + 0.13 \cdot \omega(t)^6 + 0.19 \cdot \omega(t)^5 - 0.83 \cdot \omega(t)^4 - 0.51 \cdot \omega(t)^3 + 1.71 \cdot \omega(t)^2 + 0.23 \cdot \omega(t) - 1.13 \quad \text{(A.4)}$$

$$PC2(t) = -0.15 \cdot \omega(t)^4 + 0.09 \cdot \omega(t)^3 + 0.38 \cdot \omega(t)^2 - 0.28 \cdot \omega(t) + 0.06 \quad \text{(A.5)}$$

with $\omega(t)$ centered and scaled as in Equation 2.8. The first part of the two time series is mirrored as before so that increase and decrease of atmospheric anomalies is is identical (dashed lines, Figure 2.2b).

A.3 Bulk Parameterizations for Surface Heat and Momentum Fluxes

The atmospheric forcing fields are used to calculate surface wind stress, heat and momentum fluxes in the model. The following three subsections describe how these calculations are done at each time step in the model.

A.3.1 Surface Heat Fluxes

Non-Penetrative Flux

The surface heat flux Q [$\mathrm{W\,m^{-2}}$] is defined as positive for heat leaving the ocean. This flux consists of the following contributions (Lohmann et al., 2016):

$$Q = F_{LW}^{\downarrow} + SH + \lambda E + F_{ICE} \quad \text{(A.6)}$$

where $F_{LW}^{\downarrow}$ is the long-wave radiative flux leaving the ocean, SH is the sensible heat flux, λE is the latent heat flux and F_{ICE} is the heat flux exchanged between ocean and atmosphere during the production of sea ice (Griffies, 2012). Sensible heating is the exchange of heat between atmosphere and ocean which changes the temperature of either of these (Tipler and Mosca,

2007). It generally cools the ocean, particularly near the western boundary currents such as the Kuroshio in the northern Pacific (Griffies, 2012). Latent heating occurs when water changes phases, i.e. when it evaporates or when ice melts (Tipler and Mosca, 2007). ICE is extracted from the ice model. Sensible and latent heat fluxes [$\mathrm{W\,m^{-2}}$] are calculated using bulk formulae (Fairall et al. (1996), Equations A.7 and A.8.

$$SH = \rho_a \cdot c_p \cdot C_h \cdot U_{10} \cdot (SST - T_{10}) \tag{A.7}$$

$$\lambda E = \rho_a \cdot L_v \cdot C_e \cdot U_{10} \cdot [(0.98 \cdot q_{sat}(SST) - q_{v,10}] \tag{A.8}$$

where C_h and C_e are the unitless transfer coefficients for sensible and latent heat which are themselves functions of the fluxes described in Panofsky and Dutton (1984); Geernaert (1990), L_v is the latent heat of vaporization given as a constant (2.5×10^6 $\mathrm{J\,kg^{-1}}$; Griffies, 2012) and $q_{sat}(SST)$ is the saturation water vapour mixing ratio at the sea surface.

Penetrative Flux
This flux arises due to short-wave radiation entering through the ocean surface and being absorbed by seawater. A fraction of this radiation can penetrate below the surface ocean grid cell and depends on the optical parameters of seawater (Griffies, 2012). The short-wave radiative flux (Equation A.9) through the bottom of a the surface ocean grid cell $z = \Delta z$ is calculated using the formula in Griffies (2012).

$$F^{\downarrow}_{SW} = c_p \cdot Q(z = -\Delta z) \tag{A.9}$$

A.3.2 Surface Momentum Fluxes

The exchange of momentum through the atmosphere-ocean boundary is mainly due to turbulent processes. The ocean kinematic flux (i.e. the transport per unit area per unit time) given in Griffies (2012) is associated with the turbulent transport of momentum across the ocean surface (Equation A.10).

$$-\overline{(w' \cdot (u_{10}, v_{10}))}^{\vec{\nu}} = \frac{(\tau_x, \tau_y)}{\rho_{\vec{\nu}}} \approx \frac{(\tau_x, \tau_y)}{\rho_a} \;\mid\; \vec{\nu} = (\nu_x, \nu_y) = \vec{\tau} \cdot \frac{\partial(y, x)}{\partial(u, v)} \tag{A.10}$$

where $\vec{\nu}$ is the kinematic viscosity of sea water (El-Dessouky and Ettouney, 2002). In addition, momentum is also transported through mass exchange

across the air-sea interface since water carries non-zero momentum. However, this advective momentum exchange is ignored in this climate model (Griffies, 2012).

B

Supplementary Figures

a) EXP_{EN+LN}, i) τ_x ii) SST iii) 20°C isotherm depth

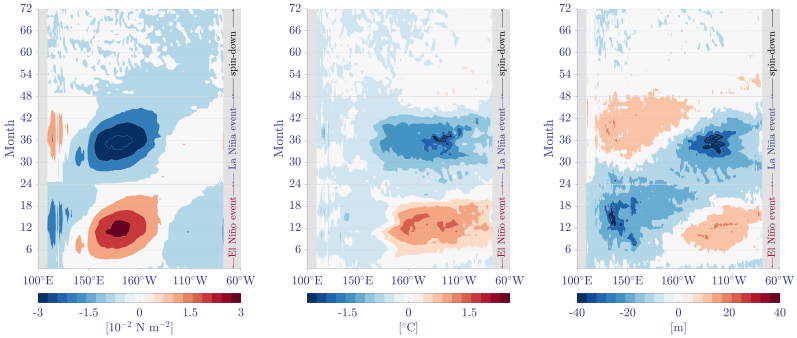

b) EXP_{LN+EN}, i) τ_x ii) SST iii) 20°C isotherm depth

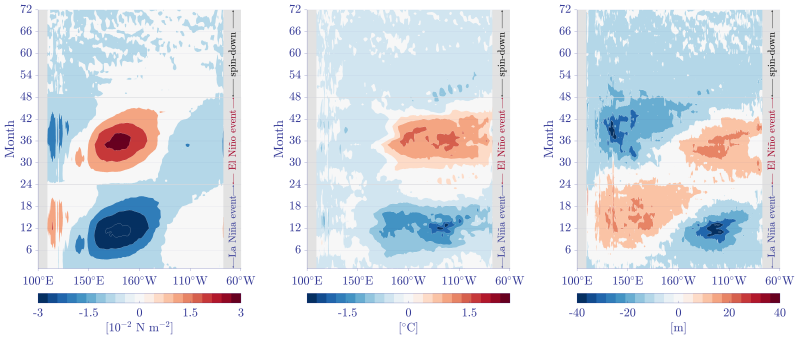

Figure B.1: Hovmoeller Diagrams during the two strong ENSO simulations a) El Niño + La Niña and b) La Niña + El Niño of i) wind stress [10^{-2} N m^{-2}], ii) SST [°C] and iii) 20°C isotherm depth [m]. Data is averaged over 5°S - 5°N.

The total volume $\mathcal{V}$ and OHC in a layer of water warmer than Θ is given by

$$\mathcal{V}(x, y, \Theta, t) = \int\int\int_{\Theta'(x,y,z,t)>\Theta} dxdydz \tag{B.1}$$

$$OHC(x, y, \Theta, t) = \rho_0 \cdot c_p \cdot \int\int\int_{\Theta'(x,y,z,t)>\Theta} \Theta' \, dxdydz \tag{B.2}$$

where Θ' is the temperature field in Cartesian coordinates (Holmes et al. (2018), Figure B.2).

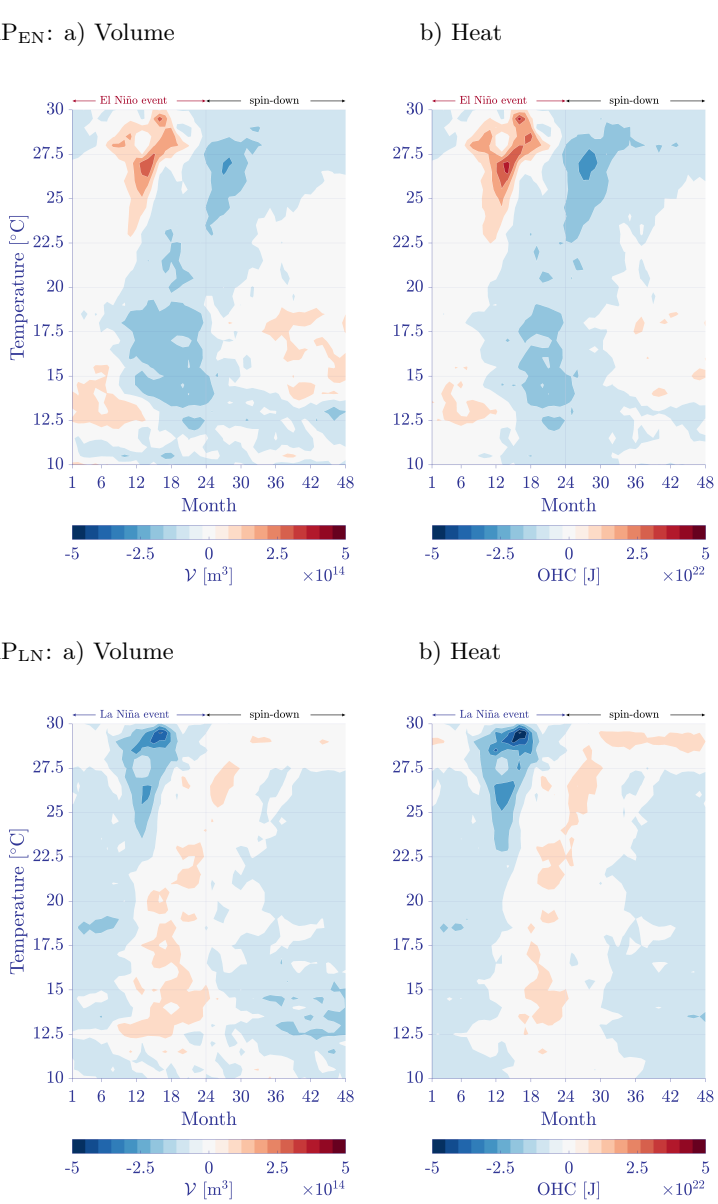

Figure B.2: In a) global volume [m^3] and in b) global heat [J] budget anomalies as a function of temperature and time for the two strong El Niño and La Niña events. The adjustments in large volumes of the colder ocean between -3°C-10°C has been omitted as this study's focus is on warm waters of the upper ocean. The correlation coefficient between OHC and $\mathcal{V}$ budget is 0.70 for the El Niño and 0.69 for the La Niña simulation. The vertical line at month 24 indicates the end of the event and subsequent start of the spin-down period.

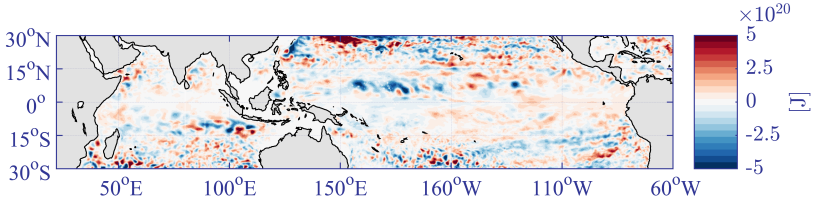

Figure B.3: Depth integrated ocean heat content anomaly difference [J] after the complete ENSO cycle, i.e. the sum of Figure 3.8a, b).

	$\mathbf{EXP_{EN+LN}}$		$\mathbf{EXP_{LN+EN}}$	
All units: $[\mathbf{10^{14}\ m^3}]$	**Recharge Phase**	Percentage	**Discharge Phase**	Percentage
Change in Warm Water Volume	+3.02	100%	−2.61	100%
Meridional transport 5°N + 5°S	+1.54	51.19%	−1.88	72.18%
Meridional transport ITF	−0.44	−14.80%	+0.43	−16.60%
Horizontal Volume Flux:	+ 1.10	**36.39** %	− 1.45	**55.58** %
$\mathcal{G}_{\mathcal{F}}$	+2.94	97.38%	−0.53	20.60%
$\mathcal{G}_{\mathcal{M}}$	−1.02	−34.01%	−0.74	28.55%
$\mathcal{J}$	−0.03	−1.32%	+0.08	−3.27%
$\mathcal{G}_{\mathcal{I}}$	+0.04	1.56%	+0.03	−1.47%
Vertical Volume Flux:	+ 1.93	**63.61** %	− 1.16	**44.42** %

Table B.1: Total contribution of each WWV budget term during the 14 month long discharge and recharge periods as defined in Figure 3.12. All values are time-integrated and in units of $[10^{14}\ \mathrm{m}^3]$. Positive (negative) values indicating volume transport into (out of) the WWV region.

a) $\mathrm{EXP}_{\mathrm{mEN+mLN}}$

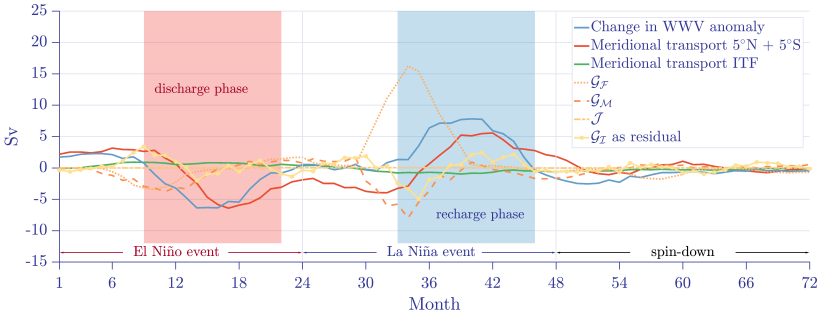

b) $\mathrm{EXP}_{\mathrm{mLN+mEN}}$

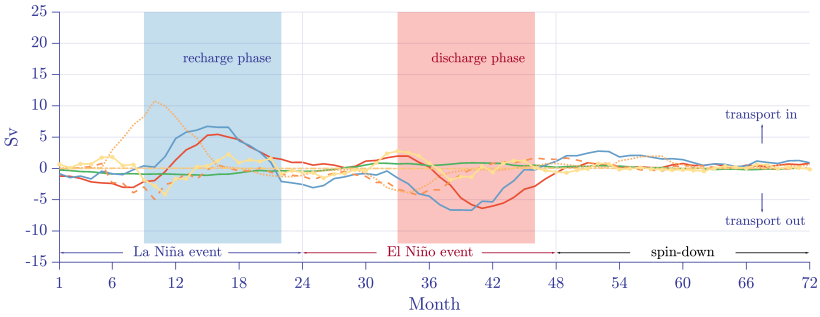

Figure B.4: The various WWV balance terms [Sv] as anomalies throughout the moderate ENSO cycle calculated in the region outlined in Figure 3.9. In a) the oscillation with El Niño followed by La Niña and in b) the ENSO cycle with a reverse order of events. A five month running mean as in Meinen and McPhaden (2000) has been applied. The discharge phase (red region in a) is defined as the time period when the change in WWV is negative from months 9–22 and the recharge period covering the same months is defined two years later (blue region). In b) discharge and recharge periods are exchanged. Positive (negative) values indicate a net transport into (out of) the WWV region as indicated on the right hand side in b). The vertical lines at month 24 and 48 indicate the end of the first and second event of the oscillation.

All units: $[10^{14}\ \mathrm{m}^3]$	Discharge Phase			
	$\mathrm{EXP}_{\mathrm{mEN+mLN}}$	Percentage	$\mathrm{EXP}_{\mathrm{mLN+mEN}}$	Percentage
Change in Warm Water Volume	−1.24	100%	−1.42	100%
Meridional transport 5°N + 5°S	−0.93	75.32%	−1.00	70.59%
Meridional transport ITF	+0.24	−19.70%	+0.24	−16.97%
Horizontal Volume Flux:		**55.61 %**		**53.62 %**
$\mathcal{G}_{\mathcal{F}}$	−0.28	22.71%	−0.41	29.01%
$\mathcal{G}_{\mathcal{M}}$	−0.40	32.49%	−0.41	28.90%
$\mathcal{J}$	+0.00	0.28%	+0.00	0.35%
$\mathcal{G}_{\mathcal{I}}$	+0.13	−11.10%	+0.16	−11.87%
Vertical Volume Flux:		**44.39 %**		**46.38 %**

	Recharge Phase			
	$\mathrm{EXP}_{\mathrm{mEN+mLN}}$	Percentage	$\mathrm{EXP}_{\mathrm{mLN+mEN}}$	Percentage
Change in Warm Water Volume	+1.75	100%	+1.26	100%
Meridional transport 5°N + 5°S	+0.88	50.67%	+0.86	68.21%
Meridional transport ITF	−0.25	−14.63%	−0.29	−23.04%
Horizontal Volume Flux:		**36.04 %**		**45.17 %**
$\mathcal{G}_{\mathcal{M}}$	+1.98	113.45%	+1.24	98.02%
$\mathcal{G}_{\mathcal{F}}$	−0.77	−44.23%	−0.44	−35.32%
$\mathcal{J}$	+0.00	0.36%	0.00	0.14%
$\mathcal{G}_{\mathcal{I}}$	−0.09	−5.62%	−0.10	−8.01%
Vertical Volume Flux:		**63.96 %**		**54.83 %**

Table B.2: Total volume transport of the individual WWV budget terms during the 14 month long discharge and recharge periods of the moderate ENSO cycles. All values are in $[10^{14}\ \mathrm{m}^3]$ with positive (negative) values indicating volume transport into (out of) the region.

C

Matlab Scripts and Model Data

The Matlab Scripts for the development of the idealized atmospheric forcing and for creating the Figures are available as an archive on the web[1]. The following three pages give more information on the Era-Interim and CNYF data sets, the key Matlab files and the ensemble setup.

[1] https://polybox.ethz.ch/index.php/s/TKbiC873I1QUUNA

Maurice Huguenin-Virchaux
08. 04. 2018, 18:33 AEDT
m.huguenin-virchaux@student.unsw.edu.au

MOM025 Notes

Atmospheric Fields for Model Input

Name	variable name @ ECMWF	resolution @ ECMWF	variable name @ CNYF	resolution @ CNYF	unit @ CNYF	filename @ RAIJIN
Zonal Wind	u10	[480, 241, 456]	U_10_MOD	[1460, 94, 192], 6h step	-24.7, 27.1 [m s^{-1}]	u_10.nc
Meridional Wind	v10	[480, 241, 456]	V_10_MOD	[1460, 94, 192], 6h step	-21.7, 20.9 [m s^{-1}]	v_10.nc
Air Temperature	t2m	[480, 241, 456]	T_10_MOD	[1460, 94, 192], 6h step	220.0, 324.48 [°C]	t_10.nc
Specific Humidity	d2m	[480, 241, 456]	Q_10_MOD	[1460, 94, 192], 6h step	-0.00, 0.03 [g kg^{-1}]	q_10.nc
Downward Longwave Radiation	strd	[480, 241, 456]	LWDN_MOD	[365, 94, 192], 1d step	106, 456 [W m^{-2}]	ncar_rad.nc
Downward Shortwave Radiation	ssrd	[480, 241, 456]	SWDN_MOD	[365, 94, 192], 1d step	0, 474.67 [W m^{-2}]	ncar_rad.nc
Total Precipitation	tp	[480, 241, 456]	PRC_MOD	[12, 94, 192], 1m step	0.1e-9, 0.00 [mm]	ncar_precip.nc
Sea Level Pressure	msl	[480, 241, 456]	SLP	[1460, 94, 192], 6h step	982, 1143 [hPa]	slp.nc

Key Matlab files

- **preparation_principle_components_and_regression_patterns_wind_....m** → regression analysis to create EOFs and PCs from the Era-Interim data
- **EXP1_preparation_anomaly_fields_mom_resolution.m** → creates regression patterns and saves them in a .nc file for later multiplication with idealized time series
- **EXP1_and_EXP2_polynomial_PC_composites_symmetric.m** → creates symmetric & idealized polynomial time series
- **EXP1_scaling_anomaly_fields_with_PCs_and_extending_time.m** → multiplying patterns with time series, adding them to CNYF and storing in .nc file
- **EXP1_and_EXP2_hovmoeller_sea_surface_temperature** → creating a Hovmöller (time vs. longitude) diagram of SST
- **EXP1_and_EXP2_depth_longitude_transect_temperature** → creating a depth-longitude figure of temperature
- **running.m** → script from where I execute my Matlab function files

Tips and Tricks cont.

showing how much storage space my files use and how much a particular folder

- *du -h --max-depth=1 /short/e14/mv7494/mom/archive*
- *du -h - -max-depth=1 ./* → shows how much space in the current folder in which the console is right now

info how much computing power I use from the allocated KSU

- *nci_account -v* → info about how much computing power I use

Tips and Tricks

splitting the time dimension of .nc files in two, i.e. extract first 1460 time steps

- *module load nco*
- ***ncrcat** -F -d TIME,1,1460, ifile ofile &*

displaying variable name in file

- *ncdump -v vname fname.nc*

executing of MOM025 model in /short/e14/mv7494/EXP...

- *module load payu*
- *payu sweep* → clears temporary files and folders
- *payu setup* → sets up archive folder for run
- *payu run* → executes the config.yaml file
- *qstat -u mv7494* → shows current status of submitted job

collating restarts, i.e. reducing their size

- *payu collate -d ../mom_perturbations/EXP.../restart00..*

moving data from the storm servers to Raijin:

- *rsync -aruv /srv/ccrc/data15/z5180028/... MSC_thesis_mom_input_EXP2_composite_nina/... mv7494@raijin.nci.org.au:/short/e14/mv7494/mom/input/... EXP2_composite_nina/*

creating monthly Era-Interim anomaly fields relative to the 1979-2008 climatology from raw 6-hourly data by detrending and removing the seasonal signal (here for u10.nc)

- *cdo -b F64 mergetime input.nc merged_u10.nc &*
- *cdo monmean merged_u10.nc monmean_u10.nc &*
- *cdo detrend -yseassub monmean_u10.nc -yseasmean -selyear,1979/2008 monmeanu10-nc anomaly_u10.nc &*

Maurice Huguenin-Virchaux
08. 04. 2018, 18:33 AEDT
m.huguenin-virchaux@student.unsw.edu.au

Data structure on Raijin server → /short/e14/mv7494/

- MOM_Anleitung → Script vom Anfang von Ryan
- mom
  - input
    - SCRAP → contains old runs
    - gfdl_nyf_1080_clean → the CNYF files
    - mom025
    - EXP1_composite_nino_windstress → input for EXP_{EN}
      - u_10_yr1.nc
      - u_10_yr2.nc
      - v_10_yr1.nc
      - ...
    - ...
  - archive
    - SCRAP → contains old runs
    - mom_control
      - [restart000, ... , restart006] → all output files
      - [output000, ... , output006]
      - pbs_logs
    - EXP1_and_EXP2_restart000_windstress → output from EXP_{EN+LN} (this is the first ensemble member, i.e. simulated from restart000)
      - [restart000, restart001, etc.]
      - [output000, output001, etc.]
      - pbs_logs
    - ...
- mom_control
  - data_table, input.nml, field_table, diag_table & config.yaml
  - archive → ../mom/archive/mom_control
- mom_perturbations
  - SCRAP (contains old runs)
  - EXP1_composite_ninos_windstress
    - data_table, input.nml, field_table, diag_table & config.yaml
    - archive → ../mom/archive/EXP1_and_EXP2_.../windstress...
  - ...

Data structure on CCRC server → /srv/ccrc/data15/z5180028/

- ProposalTemplate_14082017_0825.rar
- MSC_thesis_datasets
  - era_interim_readme.m,
  - era_interim → all Era-Interim data
  - noaa.ersst.v4 → all NOAA ERSST v4 data
  - era_interim_detrend_yseasmean
  - era_interim_anomaly_fields_PYTHON → anomaly fields created with python
  - era_interim_merge → merged Era-Interim data
  - era_interim_anomaly_fields_MATLAB → anomaly fields created with matlab
  - era_interm_anomaly_fields_CDO → anomaly fields created with CDO, the ones I eventually used
- MSC_thesis_mom_output → all output files I used for analysis
  - mom_control → control experiment runs to calculate climatology
  - EXP1_composite_ninos → output from EXP_{EN}
  - ...
- MSC_thesis_mom_input
  - mom_control → input for the control experiments, i.e. CNYF
  - anomaly_fields_mom_resolution → all anomaly fields without time evolution
  - EXP1_composite_ninos → input files, i.e. CNYF + perturbation for the simulation EXP_{EN}
  - ...

Maurice Huguenin-Virchaux
08. 04. 2018, 18:33 AEDT
m.huguenin-virchaux@student.unsw.edu.au

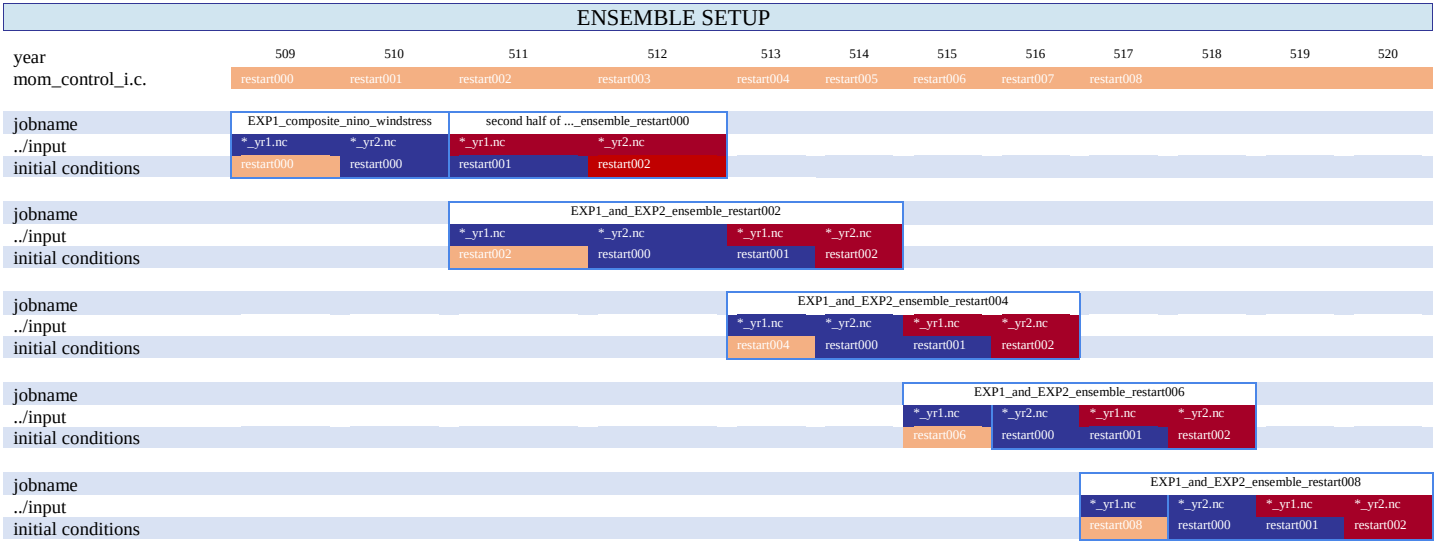

Comments:

Each run consists of a certain number of years (e.g. an El Niño simulation is two years with input for the first year (_yr1.nc) and input for the second year (_yr2.nc). After a successful simulation of one year, the initial conditions for the second year are the state of the ocean at the end of the first year (i.e. the restart file).

The ensembles are run with different initial conditions, i.e. while the first one starts at year 509, the second one starts at year 511, etc. Each ensemble run consists of four years.

The nomenclature of the individual runs on the Raijin and CCRC server are slightly different than defined in Section 2.5:

EXP1_composite_nino_windstress $\triangleq EXP_{EN}$

EXP2_composite_nina_windstress $\triangleq EXP_{LN}$

EXP1_and_EXP2_ensemble_restart000 $\triangleq EXP_{EN+LN}$ *starting at restart 000, i.e. at year 509 after spin-up of model*

D

Declaration of Originality

ETH

Eidgenössische Technische Hochschule Zürich
Swiss Federal Institute of Technology Zurich

Declaration of originality

The signed declaration of originality is a component of every semester paper, Bachelor's thesis, Master's thesis and any other degree paper undertaken during the course of studies, including the respective electronic versions.

Lecturers may also require a declaration of originality for other written papers compiled for their courses.

I hereby confirm that I am the sole author of the written work here enclosed and that I have compiled it in my own words. Parts excepted are corrections of form and content by the supervisor.

Title of work (in block letters):

Mechanisms Driving Ocean Heat Uptake and Warm Water Volume Variability Over Idealized ENSO Events

Authored by (in block letters):

For papers written by groups the names of all authors are required.

Name(s):	**First name(s):**
Huguenin-Virchaux	Maurice

With my signature I confirm that

- I have committed none of the forms of plagiarism described in the 'Citation etiquette' information sheet.
- I have documented all methods, data and processes truthfully.
- I have not manipulated any data.
- I have mentioned all persons who were significant facilitators of the work.

I am aware that the work may be screened electronically for plagiarism.

Place, date	**Signature(s)**
9th April 2018	M. Huguenin-Virchaux

Bibliography

Ashok, K., Behera, S. K., Rao, S. A., Weng, H., and Yamagata, T. El Niño Modoki and its possible teleconnection. *Journal of Geophysical Research: Oceans*, 112(C11), 2007. doi: 10.1029/2006JC003798.

Bjerknes, J. Atmospheric teleconnections from the equatorial Pacific. *Monthly Weather Review*, 97(3):163–172, 1969. doi: 10.1175/1520-0493(1969)097<0163:ATFTEP>2.3.CO;2.

Björnsson, H. and Venegas, S. A manual for EOF and SVD analyses of climatic data. *CCGCR Report*, 97(1):112–134, 1997.

Bolton, D. The Computation of Equivalent Potential Temperature. *Monthly Weather Review*, 108(7):1046–1053, 1980. doi: 10.1175/1520-0493(1980)108<1046:TCOEPT>2.0.CO;2.

Bosc, C. and Delcroix, T. Observed equatorial Rossby waves and ENSO-related warm water volume changes in the equatorial Pacific Ocean. *Journal of Geophysical Research: Oceans*, 113(C6), 2008. doi: 10.1029/2007JC004613.

Cai, W., Borlace, S., Lengaigne, M., Van Rensch, P., Collins, M., Vecchi, G., Timmermann, A., Santoso, A., McPhaden, M. J., Wu, L., et al. Increasing frequency of extreme el niño events due to greenhouse warming. *Nature Climate Change*, 4(2):111–116, 2014. doi: 10.1038/nclimate2100.

Cai, W., Wang, G., Santoso, A., McPhaden, M. J., Wu, L., Jin, F.-F., Timmermann, A., Collins, M., Vecchi, G., Lengaigne, M., et al. Increased frequency of extreme La Niña events under greenhouse warming. *Nature Climate Change*, 5(2):132–137, 2015. doi: 10.1038/nclimate2492.

Collins, M., An, S.-I., Cai, W., Ganachaud, A., Guilyardi, E., Jin, F.-F., Jochum, M., Lengaigne, M., Power, S., Timmermann, A., et al. The impact of global warming on the tropical Pacific Ocean and El Niño. *Nature Geoscience*, 3(6):391, 2010. doi: 10.1038/ngeo868.

Dee, D., Uppala, S., Simmons, A., Berrisford, P., Poli, P., Kobayashi, S., Andrae, U., Balmaseda, M., Balsamo, G., Bauer, P., et al. The ERA-Interim reanalysis: Configuration and performance of the data assimilation system. *Quarterly Journal of the Royal Meteorological Society*, 137(656): 553–597, 2011. doi: 10.1002/qj.828.

Delworth, T. L., Rosati, A., Anderson, W., Adcroft, A. J., Balaji, V., Benson, R., Dixon, K., Griffies, S. M., Lee, H.-C., Pacanowski, R. C., et al. Simulated Climate and Climate Change in the GFDL CM2.5 High-Resolution Coupled Climate Model. *Journal of Climate*, 25(8):2755–2781, 2012. doi: 10.1175/JCLI-D-11-00316.1.

Diaz, H. F., Hoerling, M. P., and Eischeid, J. K. ENSO variability, teleconnections and climate change. *International Journal of Climatology*, 21(15): 1845–1862, 2001. doi: 10.1002/joc.631.

Ekman, V. W. On the Influence of The Earth's Rotation on Ocean Currents. *Arkiv för Matematik, Astronomi och Fysik*, 2:1–53, 1905.

El-Dessouky, H. T. and Ettouney, H. M. *Fundamentals of salt water desalination*. Elsevier, 2002.

Fairall, C. W., Bradley, E. F., Rogers, D. P., Edson, J. B., and Young, G. S. Bulk parameterization of air-sea fluxes for tropical ocean-global atmosphere coupled-ocean atmosphere response experiment. *Journal of Geophysical Research: Oceans*, 101(C2):3747–3764, 1996. doi: 10.1029/95JC03205.

Geernaert, G. *Bulk parameterizations for the wind stress and heat fluxes*. Springer, 1990.

Griffies, S. M. Elements of the modular ocean model (MOM). Technical report, 2012.

Holmes, R. M., Zika, J. D., and H., E. M. Diathermal Heat Transport in a Global Ocean Model. 2018. In Preparation.

Iudicone, D., Madec, G., and McDougall, T. J. Water-mass transformations in a neutral density framework and the key role of light penetration. *Journal of Physical Oceanography*, 38(7):1357–1376, 2008. doi: 10.1175/2007JPO3464.1.

Jin, F.-F. An equatorial ocean recharge paradigm for ENSO. Part I: Conceptual model. *Journal of the Atmospheric Sciences*, 54(7):811–829, 1997. doi: 10.1175/1520-0469(1997)054<0830:AEORPF>2.0.CO;2.

Johnson, G. C. and Birnbaum, A. N. As El Niño builds, Pacific Warm Pool expands, ocean gains more heat. *Geophysical Research Letters*, 44(1):438–445, 2017. doi: 10.1002/2016GL071767.

Johnson, G. C. and Lyman, J. M. Oceanography: Where's the heat? *Nature Climate Change*, 4(11):956–957, 2014. doi: 10.1038/nclimate2409.

Kara, A. B., Wallcraft, A. J., Metzger, E. J., Hurlburt, H. E., and Fairall, C. W. Wind stress drag coefficient over the global ocean. *Journal of Climate*, 20(23):5856–5864, 2007. doi: 10.1175/2007JCLI1825.1.

Large, W. G., McWilliams, J. C., and Doney, S. C. Oceanic vertical mixing: A review and a model with a nonlocal boundary layer parameterization. *Reviews of Geophysics*, 32(4):363–403, 1994. doi: 10.1029/94rg01872.

Large, W. G. and Yeager, S. G. Diurnal to Decadal Global Forcing for Ocean and Sea-Ice Models: The Data Sets and Flux Climatologies. *NCAR Technical Note*, 2004. doi: 10.5065/D6KK98Q6.

Lengaigne, M., Hausmann, U., Madec, G., Menkès, C., Vialard, J., and Molines, J.-M. Mechanisms controlling warm water volume interannual variations in the equatorial Pacific: Diabatic versus adiabatic processes. *Climate Dynamics*, 38(5-6):1031–1046, 2012. doi: 10.1007/s00382-011-1051-z.

Levine, A., Jin, F. F., and McPhaden, M. J. Extreme noise-extreme El Niño: How state-dependent noise forcing creates El Niño–La Niña asymmetry. *Journal of Climate*, 29(15):5483–5499, 2016. doi: 10.1175/JCLI-D-16-0091.1.

Liu, C., Köhl, A., Liu, Z., Wang, F., and Stammer, D. Deep-reaching thermocline mixing in the equatorial Pacific cold tongue. *Nature Communications*, 7:11576, 2016. doi: 10.1038/ncomms11576.

Liu, Q.-Y., Feng, M., Wang, D., and Wijffels, S. Interannual variability of the Indonesian Throughflow transport: A revisit based on 30 year expendable bathythermograph data. *Journal of Geophysical Research: Oceans*, 120 (12):8270–8282, 2015. doi: 10.1002/2015JC011351.

Lohmann, U., Lüönd, F., and Mahrt, F. *An Introduction to Clouds: From the Microscale to Climate*. Cambridge University Press, 2016.

Lumpkin, R. and Johnson, G. C. Global ocean surface velocities from drifters: Mean, variance, El Niño–Southern Oscillation response, and seasonal cycle. *Journal of Geophysical Research: Oceans*, 118(6):2992–3006, 2013. doi: 10.1002/jgrc.20210.

Maher, N., England, M. H., Gupta, A. S., and Spence, P. Role of Pacific trade winds in driving ocean temperatures during the recent slowdown and projections under a wind trend reversal. *Climate Dynamics*, pages 1–16, 2017. doi: 10.1007/s00382-017-3923-3.

McDougall, T., Feistel, R., Millero, F., Jackett, D., Wright, D., King, B., Marion, G., Chen, C., Spitzer, P., and Seitz, S. The International Thermodynamic Equation Of Seawater 2010 (TEOS-10): Calculation and Use of

Thermodynamic Properties. *Global Ship-based Repeat Hydrography Manual, IOCCP Report*, 14, 2009.

McGregor, S., Spence, P., Schwarzkopf, F. U., England, M. H., Santoso, A., Kessler, W. S., Timmermann, A., and Böning, C. W. ENSO-driven interhemispheric Pacific mass transports. *Journal of Geophysical Research: Oceans*, 119(9):6221–6237, 2014. doi: 10.1002/2014JC010286.

McPhaden, M. J. A 21st century shift in the relationship between ENSO SST and warm water volume anomalies. *Geophysical Research Letters*, 39 (9), 2012. doi: 10.1029/2012GL051826.

McPhaden, M. J., Zebiak, S. E., and Glantz, M. H. ENSO as an Integrating Concept in Earth Science. *Science*, 314(5806):1740–1745, 2006. doi: 10.1126/science.1132588.

Meehl, G. A., Arblaster, J. M., Fasullo, J. T., Hu, A., and Trenberth, K. E. Model-based evidence of deep-ocean heat uptake during surface-temperature hiatus periods. *Nature Climate Change*, 1(7):360–364, 2011. doi: 10.1038/nclimate1229.

Meinen, C. S. and McPhaden, M. J. Observations of Warm Water Volume Changes in the Equatorial Pacific and their Relationship to El Niño and La Niña. *Journal of Climate*, 13(20):3551–3559, 2000. doi: 10.1175/1520-0442(2000)013<3551:OOWWVC>2.0.CO;2.

Meinen, C. S. and McPhaden, M. J. Interannual variability in warm water volume transports in the equatorial Pacific during 1993–99. *Journal of Physical Oceanography*, 31(5):1324–1345, 2001. doi: 10.1175/1520-0485(2001)031<1324:IVIWWV>2.0.CO;2.

Meyers, G. Variation of Indonesian throughflow and the El Niño-Southern Oscillation. *Journal of Geophysical Research: Oceans*, 101(C5):12255–12263, 1996. doi: 10.1029/95JC03729.

NOAA CPC. ENSO: Recent Evolution, Current Status and Predictions. http://www.cpc.ncep.noaa.gov/products/analysis_monitoring/lanina/enso_evolution-status-fcsts-web.pdf, 2017. [Accessed: 2017-25-06].

Panofsky, H. A. and Dutton, J. A. *Atmospheric turbulence: models and methods for engineering aplications*. John Wiley & Sons, 1984.

Rao, S. A. and Behera, S. K. Subsurface influence on SST in the tropical Indian Ocean: Structure and interannual variability. *Dynamics of Atmospheres and Oceans*, 39(1-2):103–135, 2005. doi: 10.1016/j.dynatmoce.2004.10.014.

Reynolds, R. W., Smith, T. M., Liu, C., Chelton, D. B., Casey, K. S., and Schlax, M. G. Daily high-resolution-blended analyses for sea surface temperature. *Journal of Climate*, 20(22):5473–5496, 2007. doi: 10.1175/2007JCLI1824.1.

Roemmich, D. and Gilson, J. The global ocean imprint of ENSO. *Geophysical Research Letters*, 38(13), 2011. doi: 10.1029/2011GL047992.

Ropelewski, C. F. and Jones, P. D. An extension of the Tahiti–Darwin southern oscillation index. *Monthly Weather Review*, 115(9):2161–2165, 1987. doi: 10.1175/1520-0493(1987)115<2161:AEOTTS>2.0.CO;2.

Saji, N., Goswami, B., Vinayachandran, P., and Yamagata, T. A dipole mode in the tropical Indian Ocean. *Nature*, 401(6751):360, 2017. doi: 10.1038/43854.

Smith, S. R., Brolley, J., O'Brien, J. J., and Tartaglione, C. A. ENSO's impact on regional US hurricane activity. *Journal of Climate*, 20(7):1404–1414, 2007. doi: 10.1175/JCLI4063.1.

Smith, T. M. and Reynolds, R. W. Extended reconstruction of global sea surface temperatures based on COADS data (1854–1997). *Journal of Climate*, 16(10):1495–1510, 2003. doi: 10.1175/1520-0442-16.10.1495.

Sprintall, J. and Révelard, A. The Indonesian Throughflow response to Indo-Pacific climate variability. *Journal of Geophysical Research: Oceans*, 119 (2):1161–1175, 2014. doi: 10.1002/2013JC009533.

Sprintall, J., Gordon, A. L., Koch-Larrouy, A., Lee, T., Potemra, J. T., Pujiana, K., and Wijffels, S. E. The Indonesian seas and their role in the coupled ocean–climate system. *Nature Geoscience*, 7(7):487, 2014. doi: 10.1038/ngeo2188.

Stewart, R. H. *Introduction to Physical Oceanography*. Texas A & M University, 2008.

Stuecker, M. F., Jin, F.-F., Timmermann, A., and McGregor, S. Combination Mode Dynamics of the Anomalous Northwest Pacific Anticyclone. *Journal of Climate*, 28(3):1093–1111, 2015. doi: 10.1038/ngeo1826.

Tipler, P. A. and Mosca, G. *Physics for Scientists and Engineers*. Springer-Verlag, 2007.

Walin, G. On the relation between sea-surface heat flow and thermal circulation in the ocean. *Tellus*, 34(2):187–195, 1982. doi: 10.3402/tellusa.v34i2.10801.

Wang, Y., Gozolchiani, A., Ashkenazy, Y., and Havlin, S. Oceanic El-Niño wave dynamics and climate networks. *New Journal of Physics*, 18(3):21–33, 2016. doi: 10.1088/1367-2630/18/3/033021.

Wyrtki, K. and Meyers, G. The trade wind field over the Pacific Ocean. *Journal of Applied Meteorology*, 15(7):698–704, 1976. doi: 10.1175/1520-0450(1976)015<0698:TTWFOT>2.0.CO;2.

Yang, Y., Xie, S.-P., Wu, L., Kosaka, Y., Lau, N.-C., and Vecchi, G. A. Seasonality and predictability of the Indian Ocean dipole mode: ENSO forcing and internal variability. *Journal of Climate*, 28(20):8021–8036, 2015. doi: 10.1175/JCLI-D-15-0078.1.